TOPICAL REVIEW

In situ biosensing technologies for an organ-on-a-chip

Biofabrication

TOPICAL REVIEW

In situ biosensing technologies for an organ-on-a-chip

Jinyoung Kim[1,5], Junghoon Kim[1,5], Yoonhee Jin[2,*] and Seung-Woo Cho[1,3,4,*]

[1] Department of Biotechnology, Yonsei University, Seoul 03722, Republic of Korea
[2] Department of Physiology, Yonsei University College of Medicine, Seoul 03722, Republic of Korea
[3] Institute for Basic Science (IBS), Center for Nanomedicine, Seoul 03722, Republic of Korea
[4] Graduate Program of Nano Biomedical Engineering (NanoBME), Advanced Science Institute, Yonsei University, Seoul 03722, Republic of Korea
[5] These authors contributed equally to this work.
[*] Authors to whom any correspondence should be addressed.

E-mail: yoonheejin@yuhs.ac and seungwoocho@yonsei.ac.kr

Keywords: organ-on-a-chip, biosensing technique, multi-organ model, real-time monitoring

RECEIVED
19 December 2022

REVISED
22 June 2023

ACCEPTED FOR PUBLICATION
25 July 2023

PUBLISHED
17 August 2023

Abstract

The *in vitro* simulation of organs resolves the accuracy, ethical, and cost challenges accompanying *in vivo* experiments. Organoids and organs-on-chips have been developed to model the *in vitro*, real-time biological and physiological features of organs. Numerous studies have deployed these systems to assess the *in vitro*, real-time responses of an organ to external stimuli. Particularly, organs-on-chips can be most efficiently employed in pharmaceutical drug development to predict the responses of organs before approving such drugs. Furthermore, multi-organ-on-a-chip systems facilitate the close representations of the *in vivo* environment. In this review, we discuss the biosensing technology that facilitates the *in situ*, real-time measurements of organ responses as readouts on organ-on-a-chip systems, including multi-organ models. Notably, a human-on-a-chip system integrated with automated multi-sensing will be established by further advancing the development of chips, as well as their assessment techniques.

1. Introduction

The development of key technologies that mimic the shape and function of an organ represents the top priority of regenerative and precision medicine. Transitioning from the simple two-dimensional (2D) culture comprising organ-derived cells, the technologies involving three-dimensional (3D) cultures are being developed to mimic the biological and physiological features of organs, including their microenvironmental niches and biochemical gradients (e.g. hormones) [1–5]. Organs-on-chips that are based on microfluidic systems allow the fine control of a fluid flow for the transfer of biochemical factors (e.g. nutrients, growth factors, and oxygen) and recapitulate the 3D organ microenvironment [6–9]. Organs-on-chips can be designed to mimic almost any organ, and the responses of organs to external stimuli or drugs can be simulated *in vitro* [10–14]. Presently, more promising and complex organ-on-a-chip systems are being developed using organoids that are generated *via* the differentiation of human stem cells and self-organization [15–19]. However, for successful implementation of organ-on-a-chip technology, the development of suitable biosensing technologies that can precisely detect biological signals in these systems is also essential.

Some widely employed characterization methods for analyzing cells in an organ-on-a-chip system include biomarker quantification, such as enzyme-linked immunosorbent assay and quantitative polymerase chain reaction, and imaging analyses, such as immunostaining, which are mostly limited to end-point assays [20, 21]. Although these methods are valuable for identifying *in vitro* organ characteristics and their biological properties, they require the destruction of the samples, making them inappropriate for measuring long-term organ responses to external stimuli. Additionally, they are inefficient and arduous. Thus, to resolve the aforementioned shortcoming, several research groups have focused on developing integrated biosensors for the *in situ*, prolonged, continuous, and noninvasive monitoring of the parameters of interest [22–25]. In addition to microscopy and off-chip analysis schemes, a range of biochemical, optical, and electrical biosensing

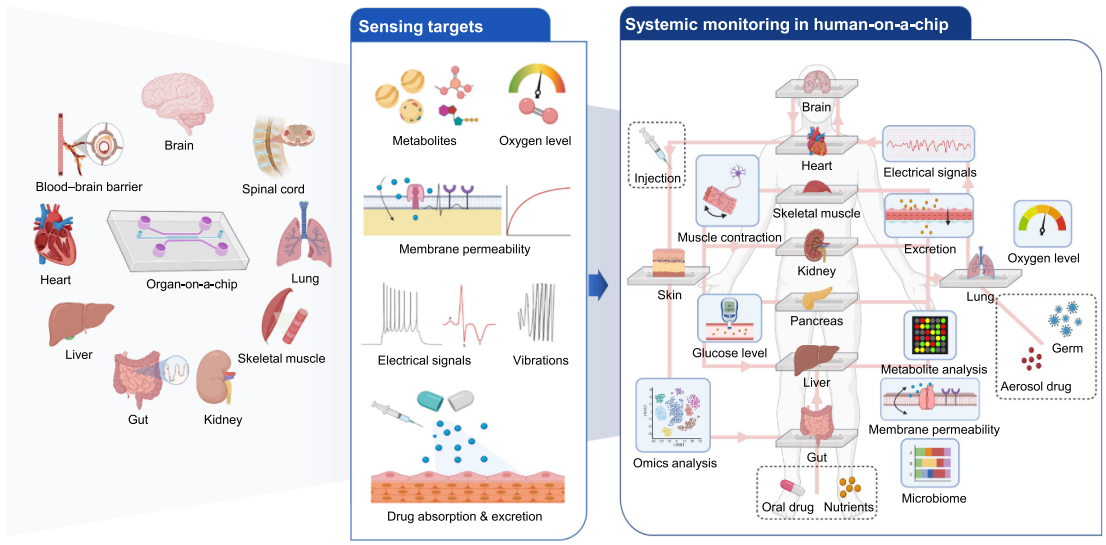

Figure 1. *In situ* biosensing targets and systems embedded in organ-on-a-chip platforms: from single-organ 3D culture models to human-on-a-chip platforms with multiple organ modules. Figure 1 was created employing biorender.com.

approaches have been reported for monitoring 3D cellular constructs within microfluidic systems. Integrated biosensors in organs-on-chips ensure rapid, real-time detection, as well as efficient screening. In a recent breakthrough, multiple organs were modeled on a single platform. Multi-organs-on-chips allow the monitoring of the potential interaction between organs, as well as the systemic modeling of diseases, by availing cross-organ communication [7, 26, 27]. The techniques that facilitate the simultaneous monitoring of multiple-organ systems, both collectively and separately, are even more complicated because the conventional analysis methods are inefficient in simultaneously sensing multiple signals and decoupling each signal for accurate interpretation.

In this review, we first introduce the *in situ* sensing methods for monitoring the various substances, permeabilities, and biological signals in organ-on-a-chip systems (figure 1). Organ-on-a-chip biosensors can be categorized into three main groups, namely electrochemical, optical, and electrical biosensors, based on their transducer types. We also review scalable sensing in organ-on-chip employing high-throughput screening (HTS) and high-content screening (HCS) technologies or omics analysis. Finally, we describe the multi-sensing technology and sensor systems employed in multi-organs-on-chips.

2. Biosensors for the 3D cell-culture model and the organs-on-chips

2.1. Sensing methods for detecting metabolic activities

All the cells in the body produce and consume a variety of substances *via* metabolism. The identification of metabolites can signal a functioning or damaged cell. Cell activity can be monitored by measuring the pH, as well as the oxygen, glucose, and lactate levels, which are the most basic substances that are associated with oxygen metabolism. The measurement of metabolites can reveal the physiological and pathophysiological information about the living state of organs and their responses to external stimuli from electrical, chemical, and physical factors. Further, metabolites can be measured in disease models to confirm, for example, whether the drugs are therapeutically effective or cause any side effects or immune responses. Therefore, in this review, we discuss the representative electrical, electrochemical, and optical sensing methods for measuring metabolites from 3D cultures and organs-on-chips (table 1).

2.1.1. Electrochemical biosensing

Electrochemical sensors transduce biochemical events into measurable electrochemical signals. In this type of sensing, an electrode is employed as solid support for the immobilization of the target biorecognition molecules. The interaction between an analyte and electrode induces changes in the electrical properties, which are usually the current flowing between the electrodes or the potential difference between the electrodes. The most common metabolic analytes include oxygen, lactate, glucose, and oxygen species; pH is the most common metabolic indicator [28, 29]. For example, breast cancer spheroids have been cultured on a chip, after which electrochemical sensors were employed to measure their oxygen, lactate, and glucose concentrations [30]. Employing chronoamperometry, the oxygen sensor measured the reduction of the molecular oxygen that was dissolved in the electrolyte. The lactate and glucose sensors

Table 1. Sensing methods for detecting metabolic events.

		Organ model	Sensing target	Material & technique	Limit of detection	References
Electrochemical	Amperometric	Liver (HepaRG hepatic spheroids)	Lactate, Oxygen	Pt electrode	Lactate: 5 μM, Oxygen: N.A.	[28]
	Amperometric	Liver (rat primary hepatocytes)	Oxygen, Oxygen consumption rate (OCR)	Inkjet-printed Ag/Au electrode	Oxygen: 0.11 ± 0.02 mg l^{-1}	[29]
	Amperometric	Tumor (BCSC1 tumor spheroids)	Lactate, Glucose, Oxygen	Ag/AgCl electrode	Oxygen: < 1 μM, Glucose: 7.6 ± 3.7 μM, Lactate: 6.1 ± 4.2 μM	[30]
	Amperometric	Muscle (C2C12)	Mouse IL-6, TNF-α	Au electrode	IL-6: 8 ng ml^{-1}, TNF-α: 2 ng ml^{-1}	[31]
	Amperometric	Breast tumor (MCF-7)	Lactate	Graphene/Pt electrode	Lactate: 0.005 μg ml^{-1}	[32]
	Amperometric	Liver (HepG2/C3A derived hepatic spheroids)	Lactate, Glucose	Pt electrode	N.A.	[35]
	Coulometric	Intestine (Caco-2)	Lactate dehydrogenase (LDH)	Au/bio-based redox capacitor (BBRC) electrode	N.A.	[33]
	Voltammetric	Midbrain (hiPSC-derived midbrain organoids)	α-Synuclein	Au electrode	$\leqslant$10 pg ml^{-1}	[34]
Optical	Luminescence	Liver (HepG2/C3A hepatic spheroids)	Oxygen	Polystyrene microbeads loaded with ruthenium-based phosphorescence dye (CPOx-50-RuP)	N.A.	[35]
	Luminescence	Lung (A549)	Oxygen, pH	OHC12 dye/Egyptian blue (pH), ptBS particle with PtTPTBPF dye (oxygen)	N.A.	[36]
	Luminescence	Stomach (hESC-derived fundic type gastric organoids)	pH	5(6)-carboxylic acid SNARF-5F	pH: 5–8	[37]
	Luminescence	Liver (HepG2)	Oxygen	PtOEP dye	0.01 ppm	[38]
	Luminescence	Lung (A594, hASC, HUVEC)	Oxygen	PtTPTBPF dye	N.A.	[39]
	Luminescence	Intestine (Caco-2)	Oxygen	PtTFPP dye	N.A.	[40]
	Luminescence	Intestine (human primary intestinal organoids, Caco-2)	Oxygen	Oxygen-sensing nanoparticles (OXNANO)	N.A.	[41]
	Luminescence	Adipose (human adipocytes)	Fatty acid	BODIPY™ 500/510 C1, C12 dye	N.A.	[44]
	Colorimetric	Lung (16HBE)	Cytokines	Nanoporous silicon nitride photonic sensor	IL-1β: 1.5 ng ml^{-1}, CRP: 3.1 ng ml^{-1}, IL-6: 7.6 ng ml^{-1}, IL-8: 20.7 ng ml^{-1}	[42]
	Fluorescence	Intestine (HIMEC, Caco-2 intestine organoids)	Oxygen	Commercially available oxygen-sensitive particles	N.A.	[43]
	Image sequences	Human red blood cells	RBC perfusion	Time lapse microscopy video analysis	N.A.	[45]

HepG2/C3A; human hepatoma cell line, MCF-7; human breast cancer cell line, C2C12; murine skeletal myoblast cell line, CM; cardiomyocytes, BCSC1; human breast cancer cell line 1, Caco-2; human colon tissue derived epithelial cells, A594; human alveolar basal epithelial cell line, HepaRG; human hepatic progenitor cell line, hASC; human adipose stromal/stem cells, HUVEC; human umbilical vein endothelial cells, HIMEC; human intestinal microvascular endothelial cells, RBC; red blood cells, 16HBE; human bronchial epithelial cells.

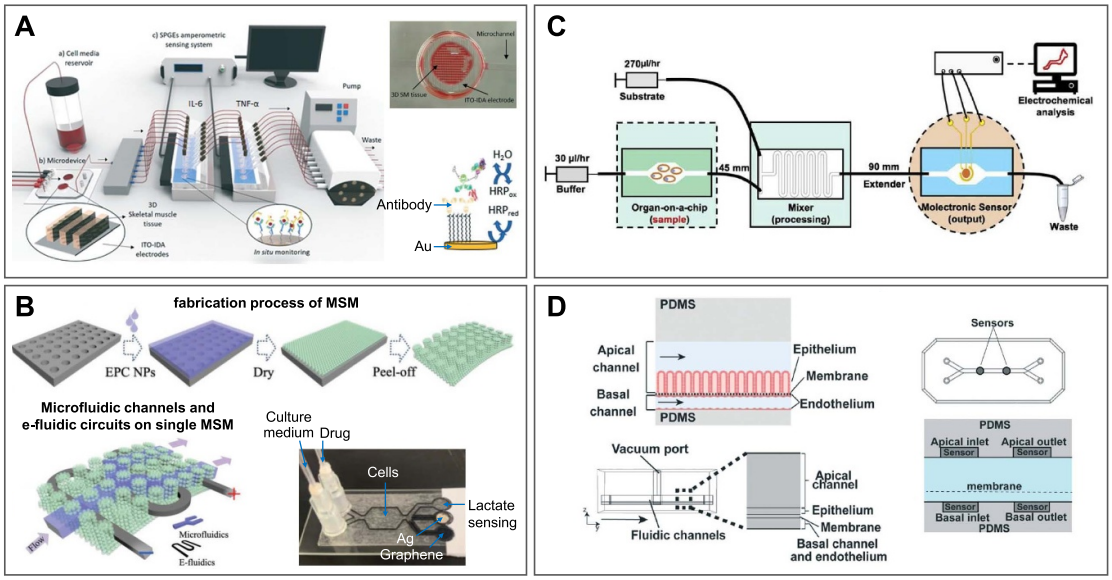

Figure 2. Organ-on-a-chip systems comprising metabolite-sensing platforms. (A) Schematic and function of the automated muscle-on-a-chip system that can electrically (using electrodes) or biologically stimulate cells and detect released cytokines *via* an electrochemical sensor. Reproduced from [31] with permission from the Royal Society of Chemistry. (B) Metastructured membrane (MSM)-based organ-on-a-chip device for detecting lactate levels. The membrane comprises ordered microstructures and nanostructures that exhibit spontaneous liquid transfer and enhances fluorescence intensity. [32] John Wiley & Sons. © 2019 WILEY-VCH Verlag GmbH & Co. KGaA, Weinheim. (C) Modular connected organ-on-a-chip platform equipped with an electrochemical sensing system to monitor the release of biological substances, such as cytotoxic molecules (e.g. LDH). Reprinted from [33], Copyright (2019), with permission from Elsevier. (D) Intestine organ-on-a-chip platform equipped with an oxygen-gradient sensor that monitors oxygen levels while maintaining the oxygen gradient that is perpendicular to the epithelial barrier. Reproduced from [41] with permission from the Royal Society of Chemistry.

were based on the conversions of lactate or glucose into hydrogen peroxide employing lactate oxidase or glucose oxidase, respectively, which was entrapped in the electrode-embedded hydrogel. The hydrogen peroxide, which was generated inside the hydrogel, was electrochemically active and could be oxidized at a constant voltage to produce a current that is proportional to the metabolite (lactate or glucose) level. By controlling the medium flow, the decrease in the oxygen levels, as well as the production of lactate, could be confirmed according to the cell activity in the cancer spheroids. Moreover, continuous measurement was possible for 1 week without any decrease in sensitivity. Therefore, built-in electrochemical sensors for continuously tracking the metabolic state of the spheroids were successfully developed on a chip.

Further, electrochemical sensing methods are generally employed to monitor immune responses and detect immune-related molecules. Ortega *et al* measured the immune substances that were generated in response to the electrical and physiological stimuli that were applied to a muscle-on-a-chip in real time (figure 2(A)) [31]. Furthermore, C2C12 cells were encapsulated in gelatin methacryloyl and a carboxymethyl cellulose methacrylate hydrogel and micropatterned *via* a photo-mold patterning technique to create 3D skeletal muscle constructs that were similar to *in vivo* tissues. The cell-culture medium was passed through a device that could measure interleukin 6 (IL-6) and tumor necrosis factor alpha (TNF-α) in real time using a screen-printed gold electrode surface on which the monoclonal antibodies were immobilized. IL-6 and TNF-α, which are secreted by skeletal muscle cells, play crucial roles in metabolism, angiogenesis, and muscle regeneration. The secretions of IL-6 and TNF-α cytokines from the 3D muscle construct, following electrical and biochemical stimulations, were confirmed employing the described electrochemical sensor. Electrical stimulation was applied employing indium–tin–oxide (ITO) interdigitated array electrodes, which were placed beneath the 3D muscle construct, and biochemical stimulation was applied by adding lipopolysaccharide (LPS). The integration of the multiplexed continual measurements of the two crucial cytokines from the 3D muscle construct allowed the investigations of inflammatory responses and regenerative processes, which can be employed as a drug-screening platform. Gao *et al* reported the electrical sensing of lactate and reactive oxygen species (ROS) using metastructured membranes that were fabricated from a micropatterned polydimethylsiloxane (PDMS) substrate comprising poly(methyl methacrylate/butyl acrylate) as the copolymer nanoparticles (figure 2(B)) [32]. The metastructured membranes comprising ordered microstructures and

nanostructures allowed liquids to flow easily through the membrane and increased the fluorescence signal. Thereafter, these membranes were employed to sense metabolites in combination with different sensing probes on a tumor-on-a-chip. The concentrations of the ROS and lactate were measured in response to real-time anticancer drug treatment. Lactate was detected employing fluorescence-based probes, and the ROS was detected *via* cyclic voltammetry employing graphene-coated electrodes to impart conductivity, followed by platinum nanoflowers to increase its catalytic efficiency. Upon administering anticancer drug treatment to the breast cancer cell line (MCF-7), a decrease and increase in the lactate and ROS levels were observed, respectively, verifying the anticancer effect of the drug in a tumor-on-a-chip.

Electrochemical biosensors have also been used to monitor cytotoxicity and disease pathology on organ-on-a-chip platforms. For example, Shang *et al* devised an interconnected organ-on-a-chip system consisting of a 'molecular-electronic' sensor and other modules, such as mixers and quality-control units (figure 2(C)) [33]. In their study, the prepared sensor for detecting a specific substance by connecting multiple modules enabled the evaluation of cytotoxicity in the organ-on-a-chip containing an intestinal epithelial culture. Further, a cytotoxicity test was conducted employing a molecular-electronic-sensor-based chip system. Following the damage of the cell membrane by a drug-mimic (Triton X-100) treatment of the human epithelial colorectal adenocarcinoma cells (Caco-2), the lactate dehydrogenase (LDH), which was released from the cell cytosol, was measured as a marker for cytotoxicity. LDH is rapidly released when a plasma membrane is damaged; thus, it is generally employed as a marker for cell damage. The electrochemical redox capacitor sensor, which stores and exchanges electrons in catechol-modified chitosan, allows the real-time measurement of the ion exchange following the conversion of lactate and NAD+ to pyruvate and NADH, respectively, *via* the catalytic reaction of LDH that was released from the cell. NADH is an electron donor that charges the film in the sensing module, and this sensor measures the concentration of LDH through a signal that is generated during the electrochemical discharge of NADH. The concentration of LDH is proportional to the number of reduced catechol moieties in the sensing module. Another study by Lee *et al* demonstrated the electrochemical detection of a marker for Parkinson's disease (PD) that was modeled by patient-derived brain organoids [34]. They developed a molecularly imprinted polymer (MIP)-based electrochemical sensing system for detecting α-synuclein that is released from the brain organoids of a PD patient. Notably, α-synuclein is a major component of Lewy bodies and neurites, which are hallmarks of PD. The conductive polymers were imprinted with α-synuclein epitopes *via* electropolymerization and deposited onto the electrodes. Thereafter, the MIP-coated electrodes were subjected to cyclic voltammetry, and their electrochemical responses to α-synuclein correlated. The concentration of α-synuclein accumulating at a specific epitope could be measured in normal and patient-derived brain organoids, thus proving the usefulness of this sensor in modeling PD and potential drug testing.

2.1.2. Optical biosensing

Optical sensing methods employ various techniques, including the use of fluorescent and luminescent labels, to measure the expression or movement of metabolites. One example is the integration of luminescence-based oxygen sensor beads into multiple spheroids (HepG2/C3A) within a bioreactor, as demonstrated by Bavli *et al* [35]. Oxygen levels were measured in real-time using lifetime-based luminescence-quenching with polystyrene microbeads loaded with a ruthenium–phenanthroline-based phosphorescence dye (CPOx-50-RuP). The phosphorescence decay time of the dye decreases as the oxygen concentration decreases, enabling the measurement of oxygen levels. Additionally, real-time glucose and lactate levels were measured using commercially available amperometric sensors. In parallel, real-time glucose and lactate levels were measured using commercially available amperometric sensors. These sensors operate based on the enzymatic reactions of glucose oxidase and lactate oxidase, respectively. The enzymatic reactions produce hydrogen peroxide (H_2O_2) in amounts proportional to the concentration of the measured metabolite. The level of H_2O_2 is then detected using platinum electrodes under polarized conditions. This comprehensive monitoring system provides insights into cellular responses and metabolic activities in the spheroids. The respiration and acidification rates of the human lung carcinoma epithelial-like cell line (A549) have been confirmed employing optical sensors that are embedded in a microfluidic chip [36]. OHC12 and Egyptian blue dyes were utilized as the pH sensors, and poly-tert-butylstyrene (ptBS) particles and platinum(II)-meso-tetra (4-fluorophenyl)tetrabenzoporphyrin (PtTPTBPF) were utilized as the oxygen sensors. The fluorescence levels of the pH and oxygen sensors were measured, following the exposure of the cell line to trifluoromethoxy carbonyl cyanide phenylhydrazone, a known chemical for increasing respiration and acidification rates; the sensitivity of the sensors was confirmed through stop-flow measurements. This optical sensing method was considered biocompatible and could be employed to collect high-throughput data for simultaneous pH

and metabolite measurements. Further, this method has been employed to monitor intestinal organoids that were prepared from human-induced pluripotent stem cells (iPSCs) [37]. McCracken *et al* evaluated the secretion of acid from the fundic type gastric organoids *via* fluorescence biosensing technology to monitor the real-time luminal pH using the pH-sensitive dye, 5(6)-carboxylic acid SNARF-5F. They observed that the pH of the fundic type gastric organoids changed rapidly in response to histamine, and this was offset by a treatment employing a histamine antagonist.

Further, several studies have utilized probes that optically sense oxygen and other substances to examine cell responses [38, 39]. For example, Wang *et al* analyzed the oxygen concentration of the intestinal environment with an oxygen sensor that was fabricated from platinum tetrakis(pentafluorophenyl) porphyrin (PtTFPP) in a co-culture model comprising intestinal cells (Caco-2) and genetically modified bacteria expressing green fluorescence protein (GFP) (*E. coli* Nissle 1917) in a microfluidic device exhibiting different oxygen environments [40]. In addition to the oxygen-sensitive sensor in the device, the oxygen levels of the Caco-2 cells and genetically modified bacteria were determined *via* pimonidazole immunostaining to measure the hypoxia levels and GFP fluorescence intensity, thereby visualizing their growths, respectively. At the various oxygen concentrations within the device, the hypoxia level was estimated by measuring the pimonidazole fluorescence levels, which were normalized to the levels that were detected under a standard normoxic condition. Employing three optical methods, namely oxygen sensing, hypoxia quantification, and growth measurements, the difference between the growths of the intestinal cells and bacteria could be visually confirmed based on the oxygen concentration, and the oxygen-consumption rate of the intestinal epithelial cells (figure 2(D)) [41]. They developed an intestine-on-a-chip system comprising two channels that were divided by a porous membrane to simulate the *in vivo* intestinal environment. One channel, which simulated the internal environment of the intestine, was composed of the primary human duodenal epithelium; the other channel, which simulated the intestinal vascular system, was composed of the intestinal microvascular endothelium. *Via* computer simulation, the researchers predicted that reducing the oxygen permeability of PDMS devices by coating them with a gas-impermeable film would induce the epithelium to naturally decrease its oxygen concentration through aerobic respiration and attain steady-state oxygen levels ($<$5%). Employing this method, a hypoxic gradient, which was perpendicular to the epithelial layers, could be created. They observed that the predicted and actual oxygen concentrations, which were measured by the oxygen sensor, were similar. The oxygen concentration was quantified by a commercially available oxygen meter that was connected to an optical fiber, and the oxygen concentration of the chip was determined in relation to the optical signal. The authors demonstrated the maintenance of the villus structure of the epithelial layer and continuous vascular endothelium under hypoxic conditions, and no changes were observed in the intestinal permeability compared with the observation under the normoxic condition.

In another study, Cognetti *et al* developed a photonic biosensor-based monitoring system for inflammatory cytokines in a lung-on-a-chip system [42]. The biosensor consisted of two sets of 14 silicon nitride photonic ring resonators, with each set featuring an edge-coupled 8-waveguide array. Within the system, one input waveguide split into seven waveguides, and two ring resonators were placed on each waveguide. To optimize sensor performance by incorporating photonic sensors in close proximity to the tissue culture substrate, the researchers employed a two-channel microfluidic design. The channels were positioned on either side of the model barrier. Human bronchial epithelial cells (16HBE cell line) in the top channel were stimulated with LPS, causing secretion of cytokines (IL-6, IL-1β). The cytokines diffused into the bottom channel, where the photonic biosensor detected them in real time.

Optical sensing methods can be employed to confirm cellular activity through the uptake of fluorescent substances [43]. Rogal *et al* developed a white adipose tissue-on-a-chip system to focus on obesity, one of the most prevalent diseases in recent times [44]. They utilized the staining of a neutral lipid to evaluate the chip function. The chip consisted of a chamber in which the adipocytes that were derived from the human primary white adipose tissue were cultured, as well as a medium channel that supplied nutrients to the cells. This chip device facilitated fluorescence analysis from the bottom of the tissue chamber. Thus, it could confirm the uptake of the fluorescently stained fatty acids in real time or the observation of the lipid vacuoles and nuclei. The concentrations of the byproducts, such as glycerol and oleic acid, were also measured, although not in real time, to confirm that the chip effectively simulated the long-term functional stability of the white adipose tissue. The possibility of utilizing the chip for drug screening was demonstrated by treating the white adipose tissue-on-a-chip with the β-adrenergic agonist, isoproterenol, and the result confirmed the lipolysis-inducing effect of the drug. The authors proposed that the research on the white adipose tissue-on-a-chip will advance the research on adipocytes, which are associated with obesity that has not been efficiently studied.

Dissimilar to the studies discussed above, one study employed the optical sensing method *via* video analysis rather than utilizing a fluorescent material. In this study, Rizzuto *et al* passed abnormal red blood cells through a microfluidic chip; the cells were quickly classified in real time *via* video analysis employing deep learning analysis [45]. The targeted rare-disease model in this study was hereditary hemolytic anemia. When the red blood cells from the patients of this disease were passed through a hole that was slightly smaller than the cells, they irreparably lost their shape, and this was in contrast to the characteristic of the red blood cells from healthy donors. Video analysis could distinguish between normal and abnormal red blood cells using an optical microscope without fluorescent markers, obtaining an accuracy of ∼91%. The authors also employed this video approach to analyze the red blood cells of patients of other rare diseases, such as sickle cell, thalassemia, and hereditary spherocytosis, with an overall accuracy of 82%. The authors concluded that their video-analysis method could be employed for several applications, including the rapid identification of cardiovascular diseases and the analyses of the statuses of donated blood samples.

2.2. Measurement of permeability at the intercellular barrier

Numerous barriers in the body protect it against harmful substances. However, they can also hinder substance exchange or drug delivery between organs. To accurately mimic the *in vivo* conditions in the laboratory, these biological barriers must be modeled. Further, it must be possible to verify that these models exhibit selective barrier functions and permeabilities for molecular transfer. The blood–brain barrier (BBB) is the most challenging barrier to overcome in the body [46]; thus, it is challenging to develop drugs that can cross the BBB and act on the brain. Therefore, reconstituting the BBB models to validate the penetration of BBB by drugs is an effective method for confirming the therapeutic potentials of brain-targeting drugs [47, 48]. Other research groups have simulated the endothelial cell layer in other tissue types (*e.g.* the glomerulus in the kidney) and epithelial barriers in intestines and lungs [13, 49, 50]. The permeabilities of cell membranes at these intercellular barriers are mainly measured electrically, and electrodes are generally placed around the chip or organoid to measure the movement of the electrical signals [12]. Another less-common method assesses barrier permeability by measuring the concentration of a substance through the visual confirmation of the fluorescent molecules passing through the barrier. Table 2 summarizes an overview of organs-on-chips with integrated sensors for measurement of the permeability of intercellular barrier.

2.2.1. Permeability measurements via the electrical resistance/impedance method

The transepithelial/transendothelial electrical resistance (TEER) is the most commonly employed method for evaluating membrane permeability with an electrical device [51–55]. The impedance is measured after placing electrodes on the inner and outer cellular membranes to assess the permeability of the membranes. TEER quantifies the integrity of cellular barriers; it can be measured in real time without resulting in cell damage. Salih *et al* fabricated an organ-on-a-chip comprising a built-in TEER device consisting of ITO electrodes for the real-time examinations of models of the formations of guts, livers, and kidneys using Caco-2, HepG2, and HK-2 cell lines, respectively, with various concentrations of fetal bovine serum (FBS) in the culture medium [56]. *Via* the TEER method, they measured the pH, albumin, kidney injury molecule-1, and alkaline phosphatase levels at different times to identify the optimal FBS conditions for tight junctions and cell growth. The optimal FBS concentration of the medium in the microfluidic device was confirmed *via* the expression of several biomarkers, as well as the TEER results, and employing 5% as the FBS concentration was considered ideal for the cell growth and formation of the tight junctions.

Numerous other studies have employed the TEER method to test BBB models. For instance, Amiri *et al* produced a micro-electrical BBB (μE-BBB) chip employing TEER electrodes that were positioned on either side of the model comprising endothelial cells and astrocytes [57]. They analyzed the TEER to determine the difference between the BBB permeabilities of young and old erythrocytes. To confirm the passage of the erythrocytes, the authors deployed an indirect method employing nitric oxide (NO). Erythrocytes release NO, a substance that increases BBB permeability when subjected to high shear stress. Thus, the older the erythrocytes, the more the NO that was released; accordingly, the BBB permeability increased with the increasing age of the erythrocytes. Therefore, this study confirmed that the age-dependent changes in the BBB permeability of erythrocytes, as measured *via* the TEER, could be a biomarker of aging.

Other methods are being developed to improve the existing TEER devices. The existing TEER device is fixed to an organ-on-a-chip and can only measure a value at a fixed location. Renous *et al* overcame this limitation by developing a new device called the spatial TEER (S-TEER) [58]. The S-TEER system offers a unique capability for localized impedance measurements at multiple points within the chip. This system consists of a pair of static transparent electrodes and a pair of movable scanning electrodes, allowing for manual movement of the electrodes along the chip

Table 2. Sensing methods for measuring the permeability of intercellular barriers.

Type		Organ model	Sensing target	Material & technique	References
Electrical	TEER	Lung (hAEC), Colon (Caco-2)	Epithelial permeability	Ti/Au electrode	[51]
	TEER	Lung (16HBE14o, HMVEC-L, hAEpC)	Epithelial & Endothelial permeability	STX100M	[52]
	TEER	Retina (ARPE-19, HREC, SH-SY5Y)	Epithelial & Endothelial permeability	Ti/Pt/Ti microgroove electrode	[53]
	TEER	Placenta (BeWo)	Epithelial permeability	Au electrode	[54]
	TEER	Kidney (MDCK-II mixed with 3T3 /PKD2 Ko mouse kidney cells/HREC)	Epithelial permeability	Ag/AgCl electrode	[55]
	TEER	Intestine, Liver, Kidney epithelial tissue (Caco-2, HepG2, and HK-2)	Epithelial permeability	ITO electrode	[56]
	TEER	Blood–brain barrier (bEnd.3, C8-D1A)	BBB permeability	Au electrode	[57]
	TEER	Intestine (Caco-2)	Epithelial permeability	Top: stainless steel electrode, Bottom: Au wire	[58]
	TEER	Lung (16HBE14o, A549)	Epithelial permeability	Au, Cu covered with Ni electrode	[59]
	EIS	Intestine (Caco-2, and HT29-MTX)	Epithelial permeability	Au electrode	[60]
	TEER	Intestine (Caco-2)	Epithelial permeability	Ti/Au/Ti electrode	[123]
Electrochemical	Amperometric	Intestine (Caco-2, HUVEC)	Endothelial permeability	Pt electrode, Potassium ferricyanide (FCN)	[61]
	Amperometric	Blood vessel (HUVEC)	Endothelial permeability	Pt electrode, $[Fe(CN)6]^{4-}$	[64]
	Voltammetric	Aorta (PAEC)	Endothelial permeability	Au/Cr electrode, methyl blue (MB), Potassium ferricyanide (FCN), Hexaammineruthenium chloride (RuHex)	[62]
	Voltammetric	Blood vessel (HUVEC)	Endothelial permeability	Au/Cr electrode, Hexaammineruthenium chloride (RuHex)	[63]
Optical	Fluorescence	Lung (16HBE14o, HMVEC-L, hAEpC)	Epithelial & Endothelial permeability	0.4 kDa FITC-sodium, 70 kDa RITC-dextran	[52]
	Fluorescence	Retina (ARPE-19, HREC, SH-SY5Y)	Epithelial & Endothelial permeability	70 kDa FITC-dextran, 70 kDa RITC-dextran	[53]
	Fluorescence	Placenta (BeWo)	Epithelial permeability	20, 500 kDa FITC-dextran	[54]
	Fluorescence	Blood–brain barrier (bEnd.3, C8-D1A)	BBB permeability	10 kDa FITC-dextran	[57]
	Fluorescence	Blood–brain barrier (NHA, hCMEC/D3)	BBB permeability	4 kDa FITC-dextran	[65]
	Fluorescence	Pancreas (HUVEC, hFB, hPDAC derived tumor organoids)	Endothelial permeability	Carboxyfluorescein diacetate (CFDA-SE)	[66]
	Fluorescence	Colon (HCT-116, hCoMEC)	Drug permeability	CMCht/PAMAM-FITC nanoparticles	[67]
	Fluorescence	Tumor-blood vessel (HUVEC, HeLa tumor spheroids)	Endothelial permeability	10 kDa AlexaFluor568-dextran	[68]
	Fluorescence	Lung (MDA-MB-231, HUVEC)	Cell extravasation & Invasion	4, 40 kDa FITC-dextran	[69]
	Fluorescence	Blood–brain barrier (hNSC, hCMEC/D3, HBVP)	BBB permeability	4, 70 kDa FITC-dextran	[70]

AEC; Alveolar epithelial cells, HUVEC; human umbilical vein endothelial cells, CM; cardiomyocytes, 16HBE14o; human bronchial epithelial cell line, A594; human alveolar basal epithelial cell line, HMVEC-L; human lung microvascular endothelial cell line, hAEpC; human primary alveolar epithelial cells, ARPE-19; human retinal pigment epithelial cell line, HREC; human retinal endothelial cells, SH-SY5Y; human neuroblastoma epithelial cell line, Caco-2; human colon tissue derived epithelial cells, HepG2; human hepatoma cell line, HK-2; human proximal tubule epithelial cell line, BeWo; human placental cell line, bEND.3; mouse brain endothelial cell line, C8-D1A; mouse astrocyte cell line, HT29-MTX; human colon cancer cell line, MDCK-II; canine kidney epithelial cell line, 3T3; murine embryo fibroblast cell line, PAEC; porcine primary aorta endothelial cells, NHA; normal human astrocytes, hCMEC/D3; human cerebral microvascular endothelial cell line, MDA-MB-231; human breast cancer cell line, HCT-116; human colon cancer cell line, hCoMEC; human colonic microvascular endothelial cells, hFB; human dermal fibroblast cells, hPDAC; human pancreatic ductal adenocarcinoma cells, HeLa; human cancer cell line; hNSC; human neural stem cells, HBVP; human brain vascular pericytes.

to obtain impedance measurements at specific locations. The introduction of this feature enables the S-TEER system to measure local variations along the cellular layer in the chip and retrieve valuable spatial information that cannot be achieved using conventional fixed TEER systems. The authors employed S-TEER to confirm the intrinsic permeability of Caco-2 cells to TNF-α and ethylene glycol-bis(β-aminoethyl ether)-N,N,N′,N′-tetraacetic acid. They reported that the permeability increased with the decreasing cell concentrations and that S-TEER could also be measured to determine the concentration of cells at the desired location in an organ-on-a-chip system. Another study integrated the TEER device with the lung-on-a-chip to overcome the limitations of existing TEER monitoring systems by placing electrodes on both sides of the epithelial barrier to evaluate the lung-barrier integrity [59]. The researchers developed a micro-impedance tomography system and measured the impedance, followed by the permeability, in a lung-on-a-chip system. Contrary to the conventional TEER system, the microimpedance tomography system is only equipped with electrodes on one side of the barrier; thus, there is sufficient space on the basolateral side to allow the cyclic breathing-like movements of the lung–alveolar barrier. This system could also be used to assess the changes in breathing movements since the electrode is placed just 1 mm from the barrier. The researchers monitored the impedance reduction in real time, following the treatment with Triton X-100 to permeabilize the epithelial layer. They also revealed the changes in the impedance due to the cyclic breathing movements of the flexible membrane on which the epithelial monolayer was cultured.

Another study, which analyzed the electrical impedance but was not based on the TEER method, performed electrochemical impedance spectroscopy (EIS) to measure the electrical signals in real time. Moysidou *et al* developed a 3D tubular electroactive scaffold with poly(3,4-ethylenedioxythiophene) polystyrene sulfonate (PEDOT:PSS). Next, they simulated lumen lining with intestinal epithelial cells to develop a long intestinal model called L-Tubistor (figure 3(A)) [60]. The lamina propria in the bulk compartment was simulated with telomerase-immortalized fibroblasts. The cells were seeded in two stages, as follows: first, the fibroblasts were seeded on the scaffold, after which the intestinal epithelial cells were seeded. During the cell infiltration of the scaffold, cell growth, and tissue formation, the changes in the resistance and capacitance could be monitored over a month. The culture containing the fibroblasts and intestinal epithelial cells on a conductive scaffold promoted the reduction in the resistance levels compared with the construct comprising only one cell type; this finding confirmed that the presence of the basal layer facilitates the movement of substances through the intestinal wall of the L-Tubistor model.

2.2.2. Permeability measurements via electrochemical methods

Although rarely employed, electrochemical sensing assesses the permeability of a barrier by detecting substances after they penetrate a membrane [61, 62]. TEER measures the resistance by sensing the voltage differences on either side of the membrane. Contrarily, electrochemical methods for sensing barrier permeability can confirm the direct passage of substances. As an example of permeability measurements *via* the electrochemical sensing method, Wong *et al* fabricated an electrochemical sensing device that differed from traditional fluorescence-based assays (figure 3(B)) [63]. They developed a microfluidic vascular model comprising a cell-culture channel containing endothelial cells that mimicked the vascular layer and an adjacent collagen-gel channel that mimicked the extracellular matrix layer containing an electrode. The permeability of the vascular model was electrochemically measured *via* square-wave voltammetry employing hexaammineruthenium(III)chloride as a tracer. Compared with the permeability of the collagen gel only, that of the established vascular model was reduced by the tight junctions that were formed by the endothelial cell layer. In a related study, the endothelial permeabilities of a vascular model containing human umbilical vein endothelial cells (HUVECs) and a co-culture model of tumors (HepG2, MCF-7, and MDA-MB-231) and HUVECs were confirmed using the tracer, $[Fe(CN)_6]^{4-}$, which was oxidized in positive potential conditions (0.5 V) of the working electrode [64]. After fabricating a HUVEC monolayer on a porous polyethylene terephthalate film, a tracer, $[Fe(CN)_6]^{4-}$, was added to the model, after which the current that was generated during the oxidation was measured to sense the permeability in real time. The electrochemical images were obtained by simultaneously measuring the permeability of the HUVEC layer in a 2D shape (20×20) using 400 electrodes, and the metastasis of the cancer cells was observed. Accordingly, the changes in the vascular permeability could be detected through the interactions with the tumor; even the spatial information could be obtained *via* many electrodes.

2.2.3. Permeability measurements via the optical-sensing methods

For the optical sensing of permeability, fluorescent tracers can be attached to a specific substance to visually confirm how the substance penetrates a permeable barrier [53, 54, 65]. This method is intuitive and has been frequently employed, especially

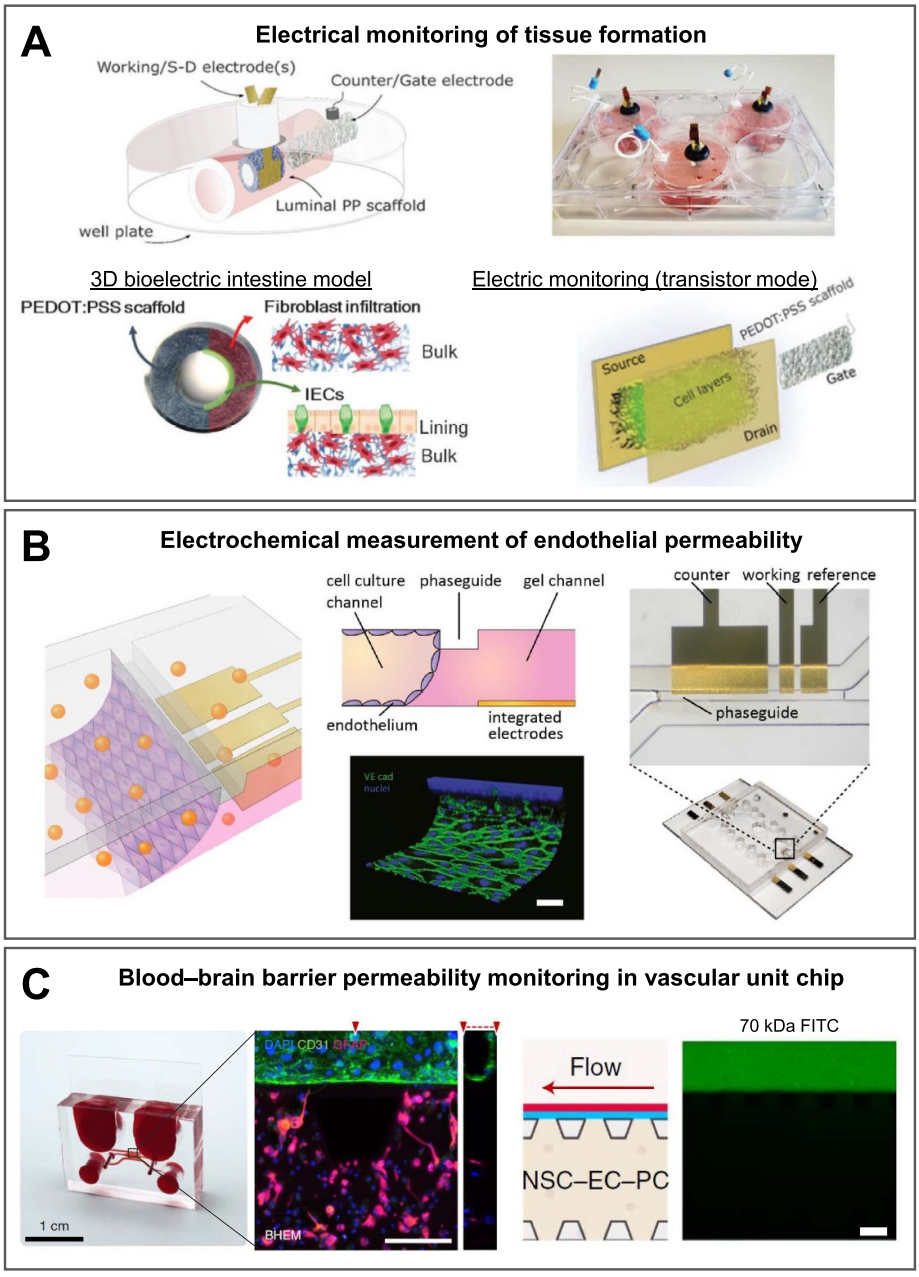

Figure 3. Organ-on-a-chip systems for examining the barrier functions of tissues. (A) Three-dimensional bioelectronic human intestine-on-a-chip platform for the real-time detection of intestinal barrier functions and elucidation of cellular activities (e.g. adhesion, proliferation, and differentiation) employing an electrochemical impedance spectroscopy monitoring system. Adapted from [60]. CC BY 4.0. © The Authors. Advanced Biology published by Wiley-VCH GmbH. (B) Schematics of the measurement of membrane permeability employing 3D hydrogel-based vascular-on-a-chip models that are equipped with electrochemical endothelial-permeability detectors. Reprinted from [63], Copyright (2019), with permission from Elsevier. (C) Monitoring the barrier functions in the 3D BBB-on-a-chip with fluorescently labeled substances. Reproduced from [70], with permission from Springer Nature.

for testing organ-function-related and nontoxic substances. For example, the intracellular transfer of small molecules into tumor cells was measured in a 3D vascularized pancreatic tumor model comprising patient-derived pancreatic tumor organoids, primary fibroblasts, and endothelial cells in a 96-well-based microfluidic device [66]. The endothelial cells were seeded on the lumen of the tubular scaffold, which spanned across the compartments and facilitated the perfusion. The co-culture comprising the pancreatic tumor organoids and fibroblasts increased the deposition of collagen on the surrounding extracellular matrix, a phenotypic hallmark of cancer, compared with the organoid culture alone. When carboxyfluorescein diacetate succinimidyl ester (CFDA-SE) was perfused through the vascularized scaffold, a slower diffusion of the small molecules was observed in the co-culture group comprising the pancreatic organoids and fibroblasts owing to the remodeled and denser matrix. These results highlight the crucial role

of fibroblasts in remodeling the stroma of pancreatic tumors.

Further, optical-sensing devices have been employed to develop drug-delivery systems. For example, Carvalho *et al* developed a colorectal tumor-on-a-chip to test the efficacy of an anticancer drug-delivery system [67]. The tumor-on-a-chip was designed for high-content image-based screening to evaluate its permeability, drug-retention, and drug-delivery systems in a gradient manner. A human colon-cancer cell line (HCT 116) was embedded in Matrigel in a circular core chamber, and human colonic microvascular endothelial cells were seeded in an adjacent channel that surrounded the core chamber. Next, gemcitabine, a chemotherapeutic drug for advanced colorectal cancer, was loaded onto fluorescently labeled carboxymethyl chitosan/poly(amidoamine) (CMCht/PANAM) dendrimer nanoparticles. The subsequent treatment employing the drug-loaded nanoparticles induced concentration-dependent cell death. In another study, Feiner-Gracia *et al* designed a cancer-on-a-chip system to evaluate the delivery and stability of self-assembled micelles comprising fluorescently labeled amphiphilic polyethylene glycol–dendron hybrid monomers [68]. The designed system comprised a channel containing HeLa cell-tumor spheroids that are embedded in collagen and a vascular channel consisting of HUVECs. First, the authors confirmed that the coculture of the two cell types induced a leaky vasculature, which was consistent with the *in vivo* pathology. Thereafter, the stability and delivery behavior of the micelles were monitored based on real-time ratiometric imaging by detecting the disassembled fluorescent monomers and assembled micelles. This imaging was performed by calculating the ratio between the emitted intensity of fluorescently labeled polymers at wavelengths of 480 nm (disassembled state) and 550 nm (assembled state). The different types of micelles exhibited different degrees and locations of accumulation in the endothelial barrier, as well as extravasation, to reach the tumor spheroids. This approach (the utilization of spectrally responsive micelles with a cancer-on-a-chip platform) can elucidate the stability and accumulation of nanoparticles and ultimately be applied to the screening of new anticancer drug-delivery systems.

Mollica *et al* developed a simple chip to model cancer-cell metastasis; they visually confirmed cell migration *via* fluorescence staining [69]. In their chip, they connected a vascular and an extravascular channel through micropillars, and this 3 μm pillar membrane effectively separated the two channels for the diffusions of the molecules and cells. Cell metastasis was examined by culturing the tumor cells on one side and culturing the endothelial cells on the other side. The functionality of the endothelial barrier was confirmed by the reduced diffusion of a fluorescent tracer (fluorescein isothiocyanate (FITC)–dextran) from the vascular to the extravascular compartments, as well as an increase in the vascular permeability by the pro-inflammatory factor (TNF-α) that was added to the extravascular compartment. Thereafter, the metastasis of MDA-MB-231 breast-cancer cells was detected by determining the number of cells that had crossed into the vascular channel through fluorescence measurements and immunostaining for intravasation and extravasation. The extravasation rate was 4 cells/day for the untreated cells; however, it increased rapidly to 12 cells/day after the TNF-α treatment, demonstrating that the established tumor-on-a-chip can simulate cancer metastasis.

The function of a BBB-on-a-chip was recently evaluated using fluorescent tracers. Kim *et al* developed a BBB-mimicking model exhibiting selective permeability between cerebrovascular cells and astrocytes on a microfluidic culture platform comprising a dynamic flow (figure 3(C)) [70]. In their study, BBB permeability varied with the presence or absence of cellular components or microfluidic flow, respectively, when FITC–dextran was administered to the vascular channel. The BBB-on-a-chip recapitulated the function of BBB *in vivo*; the treatment with an inflammatory factor (*e.g.* TNF-α) produced a loose and leaky tight junction, and the barrier function was gradually restored after the removal of TNF-α. Further, the BBB-on-a-chip system was applied to model the fungal brain infection that causes meningitis. The researchers elucidated the mechanisms of BBB penetration and neurotropism *via* the time-course fluorescence microscopy of fluorescently labeled fungi on the BBB-on-a-chip.

2.3. Biological-signal sensing on a chip

The various organs in the body generate their biological signals, including electrical (e.g. the electrical signals of the nervous system and electrical conduction of the heart) and physical (e.g. the blood pressure of the circulatory system and muscle contraction) signals. In the organ-on-a-chip field, research are ongoing to implement and measure organ-specific biological signals (table 3).

2.3.1. Electrical-signal sensing on a chip

Here, we reviewed the studies that introduced organ-on-a-chip-implemented sensors that can measure electrical signals. Moutaux *et al* developed a neural circuit-on-a-chip comprising three compartmentalized chambers (the presynaptic, synaptic, and postsynaptic compartments) and integrated it with a microelectrode-array platform (figure 4(A)) [71]. Primary cortical neurons were seeded in two opposite seeding chambers, forming oriented axodendritic

Table 3. Sensing methods for detecting biological-signals.

Type		Organ model	Sensing target	Material & technique	References
Electrical signal	Amperometric	Brain (rat primary cortical neurons)	Neuronal signals	Ti/Pt MEA	[71]
	Amperometric	Brain (hES-derived spinal cord organoid)	Neuronal signals	Commercially available MEA (Cytoview MEA 24)	[72]
	Amperometric	Heart (neonatal rat CM, hiPSC-derived CM mixed with HDF)	Cardiac field potentials	Stainless-steel needle shape electrode	[74]
	Amperometric	Heart (HL-1)	Action potentials	Pt nanopillar/Au MEA	[75]
	Amperometric	Brain (hiPSC-derived cortical organoid)	Neural activity	Pt black, 3D framework interface	[76]
	Amperometric	Heart (cardiac organoids mixed with hiPSC-derived CPC and hMSC)	Cardiac field potentials	Pt/Au nanoelectronics	[78]
	Amperometric	Brain (hiPSC-derived brain organoid)	Neuronal signals	Pt nanoelectronics	[79]
	Voltammetric	Heart (hESC-derived CM spheroid)	Cardiac field potentials	Pd/Cr/Au, 3D self-rolling microassay	[77]
	Amperometric	Heart (hiPSC-derived ventricular CM bundles)	Cardiac field potentials	Pt rod/Au electrode	[73]
Physical signal	Image sequences	Heart (hiPSC-derived ventricular CM bundles)	Muscle contraction	Motion tracking software	[73]
	Image sequences	Muscle-neuron junction (C2C12 bundles and mESC-derived MN spheroids)	Muscle twitching *via* neural activation	Optical microscopy	[80]
	Image sequences	Muscle neuron junction—motor neuron (hESC-derived MN spheroids, ALS iPSC-derived MN spheroids), muscle (hiPSC-derived skeletal myoblasts or C2C12), Blood vessel (hiPSC-derived EC)	Muscle twitching *via* neural activation	Optical microscopy	[81]
	Image sequences	Blood vessel (HUVEC)	Mimicked blood pressure	Capillary-assisted pressure sensor	[82]

hMSC; human mesenchymal stromal/stem cells, CPC; cardiac progenitor cells, HL-1; human cardiac muscle cell line, CM; cardiomyocytes, HDF; human dermal fibroblasts, ALS; amyotrophic lateral sclerosis, MN; motor neurons, C2C12; mouse myoblast cell line, HUVEC; human umbilical vein endothelial cells, EC; endothelial cells.

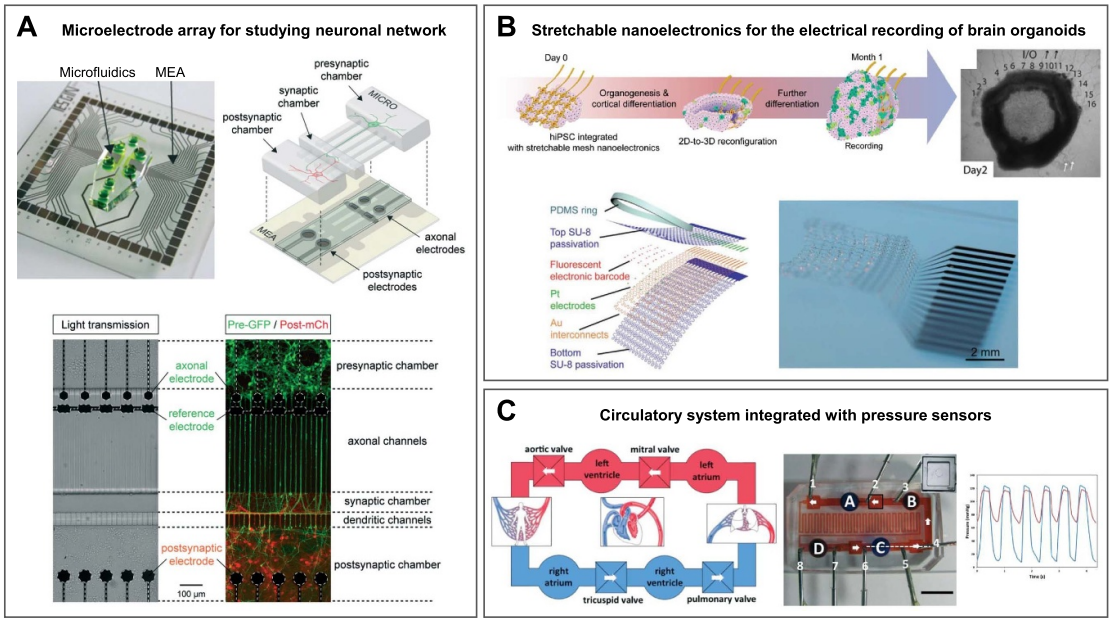

Figure 4. Organ-on-a-chip systems equipped with biological-signal-sensing platforms. (A) Morphological and electrophysiological assessments of the organized neuronal network in an organ-on-a-chip system coupled with a microelectrode-array platform. Reproduced from [71] with permission from the Royal Society of Chemistry. (B) Schematic revealing a stretchable-mesh nanoelectronic-based sensor for recording the neural activities of developing brain organoids. The sensors were integrated into the organoids during the self-organization of the 2D neural progenitors into a 3D structure. Electrical signals can be simultaneously recorded from a 16-channel device. [79] John Wiley & Sons. © 2022 Wiley-VCH GmbH. (C) Schematic configuration and a photo of a circulatory-system chip. The controllable cyclic pressure can be generated and detected. Reproduced from [82] with permission from the Royal Society of Chemistry.

synapses in the middle compartment. The device was designed to form a one-direction-oriented axo-dendritic synapse and allow electrophysiological recording. The width of the microchannels (∼3 μm) connecting the pre- or postsynaptic chamber to the synaptic chamber allowed only one neurite to traverse the synaptic chamber. Additionally, the microchannels connecting the presynaptic and synaptic chambers were longer than the maximal growth of the dendrites; thus, only axons could reach the synaptic chamber. The researchers applied a gradient coating of laminin, which exhibited the highest concentration in the post-synaptic chamber, gradually decreasing as it approached the presynaptic chamber to reduce the probability of post-synaptic axons projecting into the synaptic compartment. The electrodes were at the upper part of the microchannels near the presynaptic chamber and in the postsynaptic chamber to record or induce electrical activity. In the axodendritic network that was formed in this chip platform, different electrophysiological activities could be observed by measuring the spontaneous neuronal activities at the single-cell level, the electrical-signal transmission of the post-synaptic neuron following electrical stimulation of the presynaptic neuron, and the response of the neuronal network by the ion-channel blocker. Furthermore, Ao *et al* developed a platform for monitoring the changes in electrical signals by introducing spinal-cord organoids into a chip that was equipped with a microelectrode-array device [72]. The prolonged monitoring of the electrical signals *via* the existing microelectrode-array-based methods was impossible because the measurements are performed with only a small quantity of the culture medium to prevent the floating of the organoids in the culture medium, which could inhibit their direct contact with the electrode. To overcome this limitation, an organoid holder, such as a transwell system, was introduced to prevent the loss of contact between the organoids and electrodes. This system presents a model that can continuously monitor the electrophysiological changes in spinal-cord organoids using pain-related chemicals in a chip over a long period.

The electrical signals from the heart-on-a-chip systems have also been measured [73]. For example, Visone *et al* measured electrophysiological signals with microelectrode coaxial guide technology in a heart-on-a-chip system [74]. The microelectrode coaxial guide technology measures electrical signals by installing electrodes on both sides of the microtissue. Furthermore, the researchers developed a new platform (μHeart platform) by combining the microelectrode coaxial guide technology with a previous technology, namely μBeat, which enables a cell-culture layer and an actuation one to present a simultaneous physical beat. Since the μHeart platform enables the real-time monitoring of the electrical

signal of the organ chip, it was used to confirm maturity based on the culture times and effects of drugs, such as aspirin, sotalol, and verapamil, on the heartbeat. Further, Liu *et al* reported a monitoring platform that included a monolayer of mouse atrial HL-1 cells, micro-level extracellular electrodes in the chip, and electrodes that can facilitate nanoscale intracellular recordings to monitor the electrophysiological signals from the manufactured heart-on-a-chip [75]. The research group measured electrophysiological changes using extracellular electrodes in a heart model under acute hypoxia to determine the real-time changes in the heartbeat frequency and beat-propagation speed. Additionally, they presented a complex system that could precisely detect the action potentials of cardiac cells *via* intracellular electrode measurements.

The most recent technologies have been deployed to measure biological signals from 3D organ models. Organoids are self-assembled cell aggregates that exhibit high functionality and spatial organization of organs. A major evaluation criterion for 3D organ models includes the ability to monitor biological signals in organoids. However, a major limitation of these models is the challenge of performing the prolonged, real-time measurements of biological signals owing to the potential damage to the organ model. To overcome this limitation, researchers have developed a platform that can monitor biological signals by introducing a sensor into the 3D organ model *via* an approach that is similar to biosensing processes; the platforms are introduced into organ-on-a-chip models. A representative example is the development of a 3D framework interface; it can surround the brain and assembled organoids. The sensors-mounted microelectrodes surrounded the surface of the organoids, allowing the real-time monitoring of electrical signals from whole-brain organoids [76]. This system could be expanded by introducing additional functions, such as electrical and optical stimulations, as well as the monitoring of temperature changes and electrical-signal measurements. The development of a self-rolled cylinder-type array sensor has been reported for the overall monitoring of a 3D cardiac model [77]. In this sensor, a thin PDMS film was added before use to prevent the graphene-based microarrays from rolling; following the removal of the PDMS film during use, the array exhibited a structure that allowed self-rolling by patterns with different heights. Exploiting this self-rolling phenomenon, the array was wrapped around 3D heart organoids, and the model was mapped according to the electrical signals of the overall heartbeat-like field potential. Other studies have demonstrated a method that can facilitate the prolonged monitoring of electrical signals at various locations in the interior of 3D structures by inserting soft, nanoscale electrodes into organoids when culturing heart and brain organoids (figure 4(B)) [78, 79].

2.3.2. Physical-signal sensing on a chip

Physical signals can be measured with organ-on-a-chip systems. Uzel *et al* established a functional mouse motor unit in which muscle contraction due to nerve activity was observed on a neuromuscular junction chip [80]. To optogenetically control the electrical activity, the mouse embryonic cell line, HBG3 (expressing GFP under the control of a motor neuron-specific promoter), was knocked-in with channelrhodopsin-2, a light-gated ion channel, and differentiated into motor neurons. A PDMS-based five-channel chip design was adopted to separate the muscles and nerves. The channels at each end were used to supply the culture medium, and each adjacent channel to the medium one was separated by a neurosphere and muscle strip. The middle channel availed space for the nerves to migrate; it extended to the muscle channel. In this neuromuscular-junction structure, the muscle strips were hung on micropillars, which could be used to quantify the contractile force by calculating the degree to which the pillar was bent *via* muscle contraction. In this study, a functional *in vitro* model was demonstrated by observing and quantifying nerve activation after light stimulation and subsequent muscle contraction. In a related study, the same research group generated an optogenetic 3D human neuromuscular junction model of amyotrophic lateral sclerosis (ALS) by co-culturing human iPSC-derived muscle fiber bundles and an ALS patient's iPSC-derived motor neuron spheroids [81]. The group simplified the five-channel design into a two-channel one to separate the two of each cell type in a different channel and implemented multiple sets in one chip to enable more efficient screening of drug candidates. The light-sensitive gene, channelrhodopsin-2, was transfected into the motor neurons to control neural activity and muscle contraction. The skeletal muscle bundle was formed by injecting the cells with hydrogel in the channel exhibiting pillar structures at both ends. The muscle contractions of the ALS and healthy units, which were induced by direct electrical stimulation from the platinum electrodes or optical stimulation of motor neurons, were compared. The contraction of the muscle bundles was estimated by the deflection of the pillar structures, with the muscle bundle anchored at the ends. Compared with the healthy unit, the ALS neuromuscular junction generated less muscle-contraction force and caused myotoxicity. Furthermore, the pathological phenotype of muscle contraction–relaxation was recovered when the ALS drug candidate was administered, indicating

the potential application of this ALS neuromuscular junction model in drug screening. Furthermore, Chen *et al* measured the physical signals from organ-on-a-chip systems by developing artificial heart structures with two atria and two ventricles (figure 4(C)) [82]. They utilized a PDMS wall structure that acted as a valve that was opened and closed by the micro-pressure between each atrium and ventricle. The chip design allowed the circulation of the solution in the chip at repeated pressure, modeling the circulation system. Additionally, a capillary-assisted pressure sensor was fabricated on the chip to monitor the circulation-induced pressure changes in the channel wall. The researchers demonstrated that the blood-vessel function improved when HUVECs were cultured on the surface of the channel and when the circulating flow was applied by the micro-pressure.

3. Scalability of the sensing system on a chip

3.1. Sensing for HTS and HCS on a chip

So far, we have reviewed the extant research on the sensing of stimuli, such as substances or signals, that are generated from a small-scale, single-organ-on-a-chip system. However, the simultaneous detections of large-scale analytical systems, such as candidate-drug screening, require multi-organ-on-a-chip system. Thus, high-throughput organ chips with integrated sensors that allow HCS and HTS may be capable of translating organ-on-a-chip systems into drug discovery and development, imparting them with industrially relevant applications. Although HTS and HCS have been studied for many years, their application in organ-on-a-chip systems has only been recently highlighted (table 4).

An HTS chip can be designed by simply adding a microfluidic circuit to a commercially available cell-culture plate. Nelson *et al* developed an organ chip, following a 96-well format that mimicked the *in vivo* environment of the human bone marrow; it comprised a bone-like endosteal layer, a central bone marrow, and a perivascular niche [83]. A microfluidic circuit was fabricated based on a standard 96-well-plate format by integrating the PDMS device layer with a well plate. This strategy allowed the inclusion of eight chips in one plate and ensures compatibility with the HCS imaging systems (figure 5(A)). Employing this chip platform, the authors analyzed a hematopoietic-stem and progenitor-cell dynamics based on the presence of multi-niche-mimicked microstructures in the human bone marrow. This study revealed that the endosteal niche decreased the proliferation of the hematopoietic stem cell but increased the maintenance of the $CD34^+$ hematopoietic stem cells by monitoring the HCS images of the change in the numbers of the hematopoietic stem cell, as well as the fluorescence intensity of the $CD34^+$ expression. Additionally, radiation-exposure-induced cell apoptosis was reduced in the group containing the endosteal niche, indicating that the mimicked niche structures protected the hematopoietic stem cells from radiation damage. HCS has also been applied to study the development of lymphatic vessels, which are crucial to tumor metastasis. Lee *et al* developed a high-throughput injection-molded plastic array culture platform (Lymph-IMPACT) consisting of 28 wells per chip for fabricating lymphatic and blood vasculatures [84]. This platform facilitated the formation of self-organized lymphatic vessels, and the co-culture containing cancer cells recapitulated the cancer-type-dependent morphogenesis of the lymphatic vessels (figure 5(B)). Moreover, a co-network of the lymphatic and blood vessels could be constructed to more closely mimic the tumor microenvironment. Employing this model, the structural changes in the lymphatic vessel, which were induced by the treatment with the antitumor lymphangiogenesis drug (a VEGFR3 inhibitor), were followed by the analysis of the HCS image. The degree of the destruction of the lymphatic vessel was reduced in the blood and lymphatic co-network model compared with in the lymphatic mono-vessel model, indicating that the lymphangiogenesis in the tumor–lymphatic microenvironment was affected by the neighboring blood vessels, and this is associated with the VEGFR3 signaling pathway. Nicolas *et al* developed OrganoPlate and OrganoTEER devices, which can simultaneously measure the TEER of 40 microfluidic chips [85]. In their study, nine wells were bundled to form one microfluidic chip. With 384 wells, an OrganoPlate could simultaneously culture 40 chips (figure 5(C)). An OrganoTEER device was also developed to form an electrical circuit by penetrating four electrodes per chip. Employing these devices, the TEER of Caco-2 cells on 40 chips mounted on a 384-well plate could be simultaneously measured. The authors posited that the OrganoPlate and OrganoTEER devices were the first to measure only the cell-layer TEER without additional artificial filtration membranes. A bone-on-a-chip system was also designed for HTS and HCS in cell-culture plates [86]. In this model, an extracellular matrix, which was derived from osteoblasts (MC3T3-E1 cells), was employed as a scaffold to simulate the bone structure, and a co-culture device was fabricated to induce an interaction between the two main cell types, osteocytes and osteoblasts, that constitute the bone. The standardized chip platform was designed to mimic the shape of osteons, the functional units of bone, and was mounted on an existing commercial well plate to feature high-throughput bone units and exhibit compatibility with the HCS system. The efficacy of the anti-sclerostin antibody, a novel treatment candidate

Table 4. Sensors with scalability or to assist omics analysis.

Type		Organ model	Sensing target	Material & technique	References
Scalability	Image sequences	Blood vessel (BM-hMSC, HUVEC, BM hCD34$^+$)	Vasculogenesis pattern	PKH67 green fluorescence dye	[83]
	HCS (image sequences)	Lymphatic & Blood vessel (HDLEC, HUVEC, NHLF, SK-MEL-2, MDA-MB-231, U-87, HepG2, A549, SW480)	Lymphangiogenesis pattern	GFP fluorescence protein	[84]
	HTS (simultaneous TEER)	Intestine (Caco-2), Kidney (RPTEC)	Epithelial permeability	Stainless-steel 480 paired electrodes	[85]
	HCS (image sequences)	Bone (IDG-SW3, MC3T3-E1)	Osteoporosis pattern	Fluorescence microscopy	[86]
Omics analysis	Transcriptomics, Metabolomics	Intestine (human primary intestinal epithelium organoids)	Human microbiome metabolites (Hmm), Mouse microbiome metabolites (Mmm)	Species-specific microbiome and metabolites	[87]
	Single-cell transcriptomics, Secretomics	Pancreas (hiPSC-derived PDLOs, HPaSteCs)	Characterization of hPDLO, Co-culture effects with hHPaSteCs, PDAC biomarkers	hPDLO lysate, cultured medium (with HPaSteCs)	[88]
	Proteomics	Lung (NHBE, HPMEC)	Effect of drugs on pseudo-typed SARS-CoV-2	Cell lysates	[89]

BM-hMSC; human bone marrow mesenchymal stromal/stem cells, HUVEC; human umbilical vein endothelial cells, BM hCD34$^+$; human bone marrow CD34$^+$ cells, HDLEC; human dermal lymphatic endothelial cells, NHLF; normal human lung fibroblasts, SK-MEL-2; human melanoma cell line, MDA-MB-231; human breast cancer cell line, U-87; human glioblastoma cell line, HepG2; human hepatoma cell line, A594; human alveolar basal epithelial cell line, SW480; human colon cancer cell line, Caco-2; human colon tissue derived epithelial cells, RPTEC; renal proximal tubule epithelial cells, IDG-SW3; mouse osteoblast-to-late-osteocyte cell line, MC3T3-E1; mouse pre-osteoblast cell line, PDLO; pancreatic duct-like organoids, hPaSteC; human pancreatic stellate cells, NHBE; human bronchial/tracheal epithelial cells, HPMEC; human primary pulmonary microvascular endothelial cells.

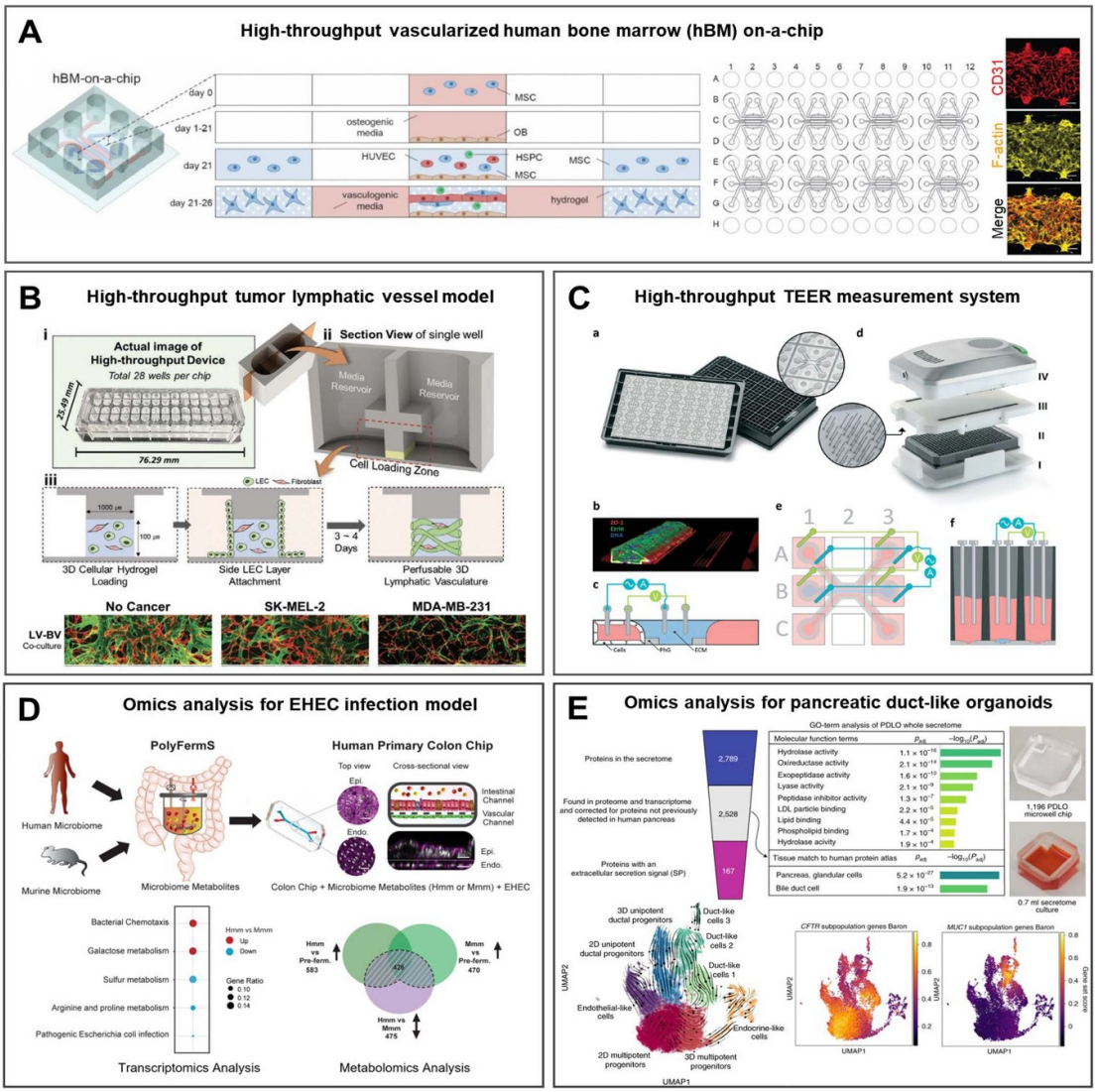

Figure 5. Scalable sensing technology and omics analysis for organ-on-a-chip systems. (A) Schematic of the high-throughput design of bone-marrow-on-a-chip recapitulating a multi-niche structure with a vasculature. The presence of mesenchymal stem cells and endothelial cells on the $CD34^{+}$ hematopoietic stem cell expansion was investigated. Reprinted from [83], Copyright (2021), with permission from Elsevier. (B) Design of the injection-molded high-throughput device for generating the 3D lymphatic network. This device can also be co-cultured with cancer cells and blood vessels to simulate a tumor microenvironment. [84] John Wiley & Sons. © 2021 Wiley-VCH GmbH. (C) Schematic of the real-time, high-throughput TEER sensing system coupled with a microtiter-plate-format-based organ-on-a-chip system. Adapted from [85]. CC BY 3.0. (D) Investigation of species-specific infection mechanisms of enterohemorrhagic *E. coli* (EHEC) using a colon chip system, coupled with omics analysis including transcriptomics and metabolomics. Adapted from [87]. CC BY 4.0. (E) Omics (singe cell RNA-sequencing, proteome and/or secretome) profiling of hiPSC-derived pancreatic duct-like organoids formed in a microwell-type chip to describe *in vitro* differentiation trajectory and identification and validation of prognostic biomarkers for pancreatic ductal adenocarcinoma. Reproduced from [88], with permission from Springer Nature.

for osteoporosis, was tested *via* HCS fluorescence imaging by analyzing the β-catenin translocation patterns. Artificial intelligence-based deep learning analysis confirmed that the bone-on-a-chip platform exhibited efficiency and accuracy in drug testing.

3.2. Omics analysis employing organ-on-a-chip systems

The emergence of omics technologies allows the analysis and interpretation of a large amount of data; it avails total information and comprehensively interprets its biological meaning beyond existing fragmentary analysis. Omics has been recently employed in the organ-on-a-chip field as an additional tool for collecting and interpreting more diverse and meaningful information than the existing sensing or simple analysis methods. Here, we review the latest research on the introduction of omics analysis to organ-on-a-chip systems.

Omics analysis was first introduced in organ-on-a-chip systems in relation to the digestive system. Tovaglieri *et al* designed a colon chip to identify enterohemorrhagic *Escherichia coli* (EHEC) infection-associated metabolites *via* metabolomic analysis and validate the pathogenicity of the microbiome *via* transcriptome analysis (figure 5(D)) [87].

The authors constructed a human colon chip exhibiting two channels by culturing human colon organoids on one side and human intestinal microvascular endothelial cells on the other. EHEC, as well as the human microbiome metabolites (Hmm) or mouse microbiome metabolites, were added to the epithelial region. The transcriptomic analysis identified the upregulation of the genes that are related to flagellar motility in Hmm-treated EHEC, and the movement of EHEC was also improved by Hmm treatment. The metabolomic analysis identified four byproducts that were highly expressed in Hmm. When the byproducts alone were utilized as a treatment, the degree of EHEC infection was similar to that of the infection in the Hmm-treated colon cells. The authors concluded that human-specific EHEC infection was caused by the high concentrations of specific metabolites present in Hmm.

Omics analysis has also been performed for a pancreas-on-a-chip system because the pancreas plays several crucial roles, including the secretions of hormones and digestive enzymes in the body. Wiedenmann *et al* developed a chip platform that could facilitate the uniform and long-term culturing of pancreatic organoids by controlling the initial sizes and shapes of the pancreatic organoids (figure 5(E)) [88]. The chip was specifically used to control cell density and number to generate uniformly sized 3D aggregates. Through time-resolved, single-cell transcriptomic analysis, the homogeneity of the chip-cultured organoids confirmed that most progenitor cells matured into two types of duct-like cells during differentiation and that the subpopulations were expressed similarly to the human adult duct cells found *in vivo*. Additionally, the cancer-specific biomarkers were determined by comparing normal pancreatic organoids with pancreatic cancer organoids on the chip platform *via* single-cell sequencing and secretomic analysis.

A recent study performed the omics analysis of a lung-on-a-chip that was infected with influenza. This lung-on-a-chip was designed with an air–liquid interface, and drugs, which were used clinically for influenza treatment, were tested for efficacy in the chip model [89]. The chip exhibited a two-channel design to simulate the cross-section of the lung, with the human bronchial airway epithelial basal stem cells cultured on one channel in contact with the air and the primary human pulmonary microvascular endothelial cells cultured on the channel supplying the culture medium. The influenza virus was administered through the air channel, and the drugs were administered through the liquid channel. The infection model was verified by analyzing the expression of several inflammatory responses, as well as monitoring the response of neutrophils that were injected into the chip. Further, proteomic analysis was performed to evaluate the efficacy of the tested drugs, and the result demonstrated that the levels of the proteins associated with cilia regulation and lysosomes increased dramatically after the treatment with the drug. The authors concluded that the drugs, which were used to block viral infections, exerted excellent therapeutic effects.

4. Multi-sensing methods for a 3D culture model and a multi-organ-on-a-chip system

4.1. Multi-sensing methods on a chip

Based on the techniques discussed above, researchers in the organ-on-a-chip field have advanced toward simulating the *in vivo* environment with multi-organ-on-a-chip systems. Since multi-organ systems generate many signals, it might be difficult to detect and quantify all the signals *via* single sensing technology [90, 91]. Thus, we reviewed studies on multi-sensing methods that can simultaneously detect multiple signals (table 5).

A simple modular platform was designed to implement multi-sensing by connecting sensing and an organ module with an automated flow-controlling breadboard (figure 6(A)) [92]. This system encompasses two chambers for the liver and heart cultures; both chambers can be continuously monitored by an electrochemical sensor (employing $K_3[Fe(CN)_6]$ to measure the levels of the secreted biomarkers) and optical sensors (to measure the pH and oxygen concentrations). Farooqi *et al*'s model represents another example of integrating multiple sensors on an organ-on-a-chip. It consists of a liver-on-a-chip system utilizing HepG2 cells coupled with devices for monitoring the changes in the pH and TEER values using photoelectric and ITO-based electrical sensors, respectively [93]. The research group employed several methods, such as live cell imaging, the quantifications of albumin and lactate productions, and E-cadherin confocal microscopy, to validate their real-time TEER data. Furthermore, the drug-induced hepatotoxicity, which was induced by doxorubicin, lapatinib, and epirubicin at various concentrations, was investigated, and the researchers observed that the doxorubicin treatment at a 1 μM dose was cytotoxic; this was confirmed by the rapid decrease in the TEER values, indicating the breakdown of the tight junctions, and an acute decrease in the pH, indicating cell death. Asif *et al* designed a proximal tubule-on-a-chip coupled with a platform for monitoring the TEER and pH values of culture media [94]. The electrodes were fabricated by printing ITO on a transparent glass chip, after which an optical pH sensor was connected to the chip to detect the color changes therein. Additionally, the cell growth was continuously monitored by an integrated microscope. The fibroblasts and HK-2 cells (immortalized proximal tubule epithelial cells) were cultured in the proximal tubule-on-a-chip and the TEER was continuously monitored by complete monolayer formation. A hyperglycemic renal nephrotoxicity model was

Table 5. Multi-sensor and multi-organ-on-a-chip systems.

Type		Organ model	Sensing target	Material & Technique	Limit of detection	References
Multi-sensors	Simultaneous TEER, Luminescence	Kidney (HRPTEC, HMVEC)	Epithelial permeability, Metabolic activity	Ag/AgCl electrode (TEER), PrestoBlue™ HS cell viability reagent (metabolic activity)	TEER: 0.22 Ωcm^2	[90]
	TEER, Voltammetric	Heart (hiPSC-derived CM, and HUVEC)	Cardiac field potentials, Endothelial permeability	Pt MEA (cardiac field potentials), Au electrode (TEER)	N.A.	[91]
	Amperometric, Luminescence, EIS	Liver (hPH spheroids, HepG2), Heart (hiPSC-derived CM spheroids)	Oxygen, pH, Temperature, Protein biomarkers	Au electrode (protein biomarker), Phenol red (pH), $[Ru(dpp)_3]^{2+}Cl_2$ (oxygen), Physitemp IT-18 Type T thermocouple Probe (temperature)	Albumin: 0.09 ng ml^{-1}, GST-α: 0.01 ng ml^{-1}, CK-MB: 0.0024 ng ml^{-1}	[92]
	TEER, Luminescence	Liver (HepG2)	pH, Epithelial permeability for drug toxicity, Albumin, Lactate	ITO electrode (TEER), Photodiode (pH), Human albumin ELISA kit (albumin), Lactate assay kit (lactate)	Albumin: 1.5 μg ml^{-1}, Lactate: N.A.	[93]
	TEER, Luminescence	Kidney (HK-2, CCD-986sk)	pH, Epithelial permeability	ITO electrode (TEER), Phenol red (pH)	N.A.	[94]
	TEER, Luminescence, Amperometric, Transcriptomics	Liver (hHSC), Retina (HRP, HRMVEC), Colon (HCoEpiC), Kidney (HRPTEC, HMVEC), Epithelial tissue (vascular EC)	Epithelial permeability, Oxygen, Active transport, Cytochrome enzymes, RNA expression change in a starvation situation	Stainless-steel electrode (TEER), FireStingO2 optical oxygen meter (oxygen), 6-CF substrate (transport), Luciferin-CYP (enzymes), Cell lysates (transcriptomics)	N.A.	[95]
Multi-organ-on-a-chips	Amperometric, Luminescence, Image sequences	Liver (HepG2/C3A), Heart (hiPSC-derived CM), Muscle-neuron junction (hSkMuSC, and hSCSC-derived MN), Brain (hiPSC-derived cortical neurons)	Cardiac beating, Myotube contraction, Neuronal signals, Cytochrome activity, Urea, Albumin	Patch clamp (electrical signals), ELISA assay kit (albumin), Cytochrome P450 assay kit (CYP1A1, CYP3A4), Urea assay kit (urea), Optic microscopy (cardiac beating, muscle contraction)	Albumin: 0.69 ng ml^{-1}, CYP1A1, CYP3A4: N.A., Urea: 13 μM	[96]
	Amperometric, Luminescence, Image sequences	Liver (hPH), Heart (hiPSC-derived CM), Muscle-neuron junction (HSkM, and hMN)	Contractile activity, Neuronal signals, Cytochrome activity, Urea, Albumin	Stainless-steel MEA (electrical signals), ELISA starter accessory kit (albumin), Cytochrome P450 assay kit (CYP1A1, CYP3A4), Urea assay kit (urea), Optic microscopy (muscle contractile)	Albumin: 0.69 ng ml^{-1}, CYP1A1, CYP3A4: N.A., Urea: 13 μM	[103]

(Continued.)

Table 5. (Continued.)

Type		Organ model	Sensing target	Material & Technique	Limit of detection	References
	Amperometric, EIS, TEER, LC-MS	Liver (liver organoids mixed with hHSC, hHP, and Kupffer cells), Heart (heart organoids mixed with hiPSC-derived CM and HCF), Lung (HMVEC-L, airway stromal cells, hBEC)	Albumin, Urea, Lactate dehydrogenase (LDH), α-GST, Membrane permeability, Cytokines, Biomarkers, Cardiac organoid beating, Metabolic profiling	ELISA assay kit (human albumin), Urea colorimetric assay (urea), Lactate dehydrogenase assay kit (LDH), α-GST Assay kit (α-GST), ELISA assay (cytokines; IL-8, IL-1β), Au electrode (biomarkers), Customized electrode (TEER), Optic microscopy (cardiac organoid beating), Cultured medium (metabolic profiling)	Albumin: 0.5 μg ml^{-1}, Urea: 13 μM, LDH: 1 mU ml^{-1}, α-GST: N.A., IL-8: 12.3 pg ml^{-1}, IL-1β: 6.5 pg ml^{-1}	[104]
	Fluorescence, Luminescence, Image sequence	Liver (HepG2, HUVEC), Tumor (MDA-MB-231), Blood vessel (HUVEC), Heart (hiPSC-derived CM), Lung (MDA-MB-231)	Permeability, Urea, Contractile activity, Cell viability	70 kDa TRITC-dextran (permeability), QuantiChrom urea assay kit (urea), Optic microscopy (cardiac contractile), CFDA dye (cell viability)	N.A.	[105]
	Amperometric, EIS	Breast cancer (SK-BR-3 spheroids), Heart (hiPSC-derived CM spheroids)	Biomarkers (troponin T, CK-MB, HER-2)	Au electrode (biomarkers)	Biomarkers: ≈0.01 pg ml^{-1}	[106]
	Fluorescence MS/MS	Intestine (Caco-2, HUVEC), Liver (hPH, hLSEC), Kidney (hRPTEC, hGMVEC), Heart (hiPSC-derived CM, HUVEC), Lung (A549, HUVEC), Blood–brain barrier (HA, hPC, HBMVEC), Brain (human hippocampal NSC), Skin (HDFa, HEKn, HDMEC)	Barrier function, Total protein quantification, Intravenously diffusion simulation	Dextran-Texas red 70 kDa, Dextran-cascade blue 10 kDa, Inulin-FITC 2–5 kDa (barrier function), Cell lysate (total protein quantification), Inulin-FITC 2–5 kDa (intravenously diffusion simulation)	Inulin-FITC 2–5 kDa: 5 ng ml^{-1}	[107]
	Fluorescence, Luminescence, TEER, MS/MS	Intestine (Caco-2, HUVEC), Bone marrow (HUVEC, human primary CD34^{+} progenitor cells), Liver (HLSMEC, hPH), Kidney (hGMVEC, hRPTEC)	Barrier functions, Endothelial permeability, Albumin, Cytochrome P450 activity, Nicotine, Cotinine, Cisplatin concentrations	Inulin-FITC, Cascade blue hydrazide trisodium salt (barrier function), Ti/Au electrode (TEER), ELISA quantitation kit (human albumin), P450 Glo kit (CYP3A4 activity), Cultured medium (drug concentration)	Albumin: 0.69 ng ml^{-1}, P450 CYP3A4: N.A., Nicotine, cotinine: 10–40 nM	[108]

(Continued.)

Table 5. (Continued.)

Type		Organ model	Sensing target	Material & Technique	Limit of detection	References
	Omics analysis (proteomics, secretomics), MSFMS, TEER, Fluorescence, Luminescence	Heart (hiPSC-derived CM, NHDF), Skin (NHDF, hKC), Liver (hiPSC-derived HC, NHDF), Bone (MSC-derived OB, Primary monocytes-derived OC, Endothelial barrier (HUVEC, MSC), Immune cells (primary $CD14^+$ monocytes)	Small molecule absorption and diffusive transport, Drug toxicity, Cytokine profiling, Tissue-specific functions, Endothelial permeability, RNA expression changes, Proteome profiling, Secretome profiling, miRNA biomarkers	3 kDa FITC-dextran (small molecule absorption and diffusion), Cultured medium (drug toxicity, cytokine, secretome profiling), Human cardiac troponin I ELISA kit (heart function), Human albumin ELISA kit, Urea nitrogen test kit (liver function), TRAP activity, Bone sialoprotein (bone function), EndOhm (TEER, skin function), Cell lysate (RNA expression, proteome profiling, miRNA biomarkers)	Troponin I: 4.4 pg ml^{-1}, Albumin: 0.69 ng ml^{-1}, Urea nitrogen: N.A., TRAP activity: N.A., Bone sialoprotein: 0.156 ng ml^{-1}	[110]

hPH; human primary hepatocytes, HepG2; human hepatoma cell line, CM; cardiomyocytes, HK-2; human proximal tubule epithelial cell line, CCD-986sk; human dermal fibroblast cell line, hHSC; human hepatic stellate cells, HRP; human retinal pericytes, HRMVEC; human retinal microvascular endothelial cells, HCoEpiC; human primary colon epithelial cells, HRPTEC; human primary renal proximal tubule cells, HMVEC; human dermal microvascular endothelial cells, HUVEC; human umbilical vein endothelial cells, HepG2/C3A; human hepatoma cell line, hSkMuSC; human skeletal muscle stem cells, hSCSC; human spinal cord stem cell line, hMN; human motor neurons„ HSkM; human skeletal myoblasts, hHCS; human primary hepatic stellate cells, HCF; human cardiac fibroblasts, HMVEC-L; human lung microvascular endothelial cells, hBEC; human bronchial epithelial cells, SK-BR-3; human breast cancer cell line, hEC; human endothelial cells, MDA-MB-231; human breast cancer cell line, Caco-2; human colon tissue derived epithelial cells, HLSMECs; human liver sinusoidal microvascular endothelial cells, hGMVEC; human primary glomerular microvascular endothelial cells, hRPTEC; human primary renal proximal tubule epithelial cells, hLSEC; human liver sinusoidal endothelial cells, A594; human alveolar basal epithelial cell line, HA; human primary astrocytes, hPC; human primary pericytes, HBMVEC; human primary brain microvascular endothelial cells, NSC; neural stem cells, HDFa; human primary adult dermal fibroblasts, HEKn; human primary neonatal epidermal keratinocytes, HDMEC; human primary dermal microvascular endothelial cells, NHDF; normal human dermal fibroblasts, hKC; human keratinocytes, HC; hepatocytes, MSC; mesenchymal stromal/stem cells, OB; osteoblasts, OC; osteoclasts.

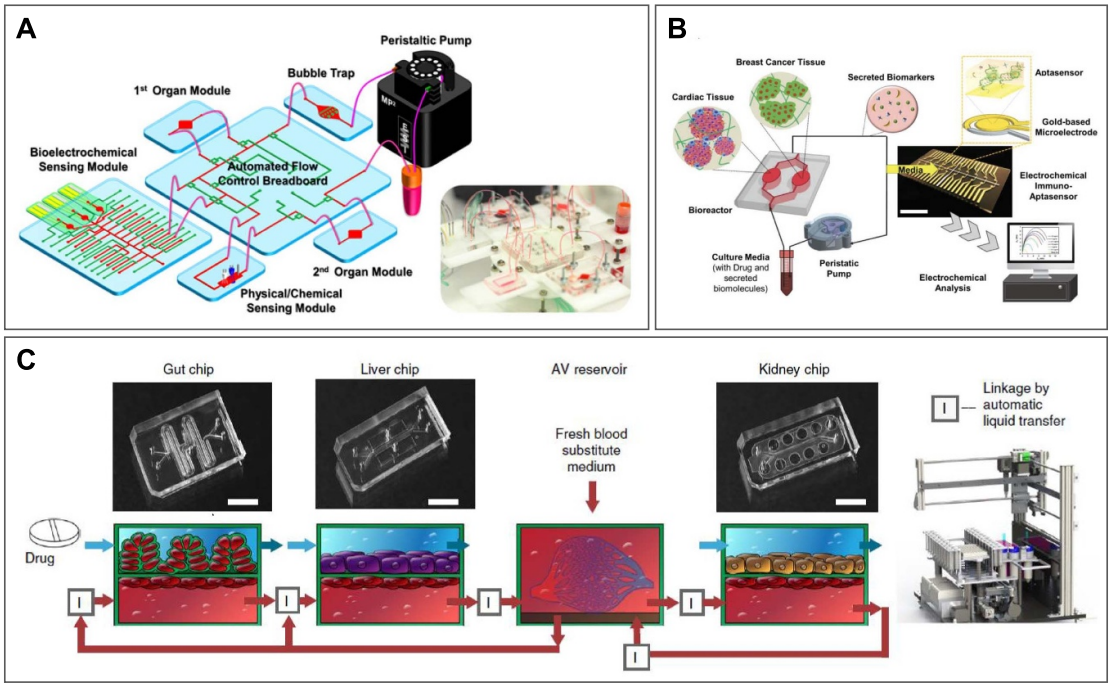

Figure 6. Multi-sensing and multi-organ-on-a-chip systems. (A) Schematics showing an automated multi-organ-on-a-chip (heart and liver) with multi-sensing platforms for detecting tissue-specific biomarkers and tissue microenvironments, such as temperature, pH, and oxygen concentrations. Reproduced with permission from [92]. (B) Schematic illustration of the cardiac–breast cancer-on-a-chip integrated with electrochemical-based multiplexed microelectrode-array platform to simultaneously monitor multiple biomarkers. [106] John Wiley & Sons. © 2020 Wiley-VCH GmbH. (C) Compartmentalized design and images of a multi-organ chip (connected gut, liver, kidney, and blood vessel) equipped with an automated circulatory system for pharmacokinetic and pharmacodynamic analysis. Reproduced from [108], with permission from Springer Nature.

induced by high-glucose treatment, which induces inflammation; afterward, the efficacy of the anti-inflammatory drug, metformin, was monitored by continuously measuring the TEER, pH, and cell growth. The high-glucose treatment decreased the impedance and caused a rapid decrease in the pH of the medium, indicating cell injury. Subsequently, the drug efficacy was confirmed by the partial restoration of the reduced impedance and pH. Another recent study exploited a high-throughput organ-chip system to make it compatible with HCS tools by adapting it into a 96-well plate configuration [95]. The researchers employed the integrated perfusion system to support complex organ functions and monitored the organ function with the TEER electrodes and oxygen sensors. Active micropumps were integrated within a plate lid, and the electrodes were embedded in the perfusion system for real-time TEER measurements within each well. The research group achieved the programmable controls of the perfusion flow, which enhanced hepatic-tissue function, and high-shear stress flow, which induced endothelial alignment.

4.2. Multi-organ-on-a-chip systems with biosensors

Since the first development of the organ-on-a-chip, the need for multi-organ chips has grown continuously (table 5). The early multi-organ chips were limited to the simple connection of several single-organ chips. For example, a four-organ-chip system (i.e. a system consisting of the heart, liver, skeletal muscle, and nervous system) was used to evaluate and compare the effects of several drugs (doxorubicin, atorvastatin, valproic acid, acetaminophen, and metacetamol), which are known to be therapeutic but become toxic at higher concentrations in animals and humans, for 14 d [96]. The functionalities of the liver, heart, skeletal muscle, and nervous system were evaluated by measuring the albumin and urea concentrations of the medium, contractile activity employing a cantilever, contractility *via* video analysis, and electrophysiological potential, respectively. The type of organ response to the administered drug closely correlates with the results of previous clinical studies [97–102]. The same group improved the multi-organ-on-a-chip model by recording the electrical and mechanical functions to monitor organ function [103]. Each organ, except for the liver, exhibited a cantilever or customized multielectrode-array module for measuring their mechanical or electrical properties, respectively. The mechanical and electrical properties of the skeletal muscle and nervous system were monitored, respectively. For the heart, its electrical and mechanical functions were evaluated with both modules. The daily mechanical and electrical measurements from the

heart, skeletal muscle, and nervous system demonstrated that the organs maintained their functions for 4 weeks, thereby enabling the study of the chronic effects of drugs.

A similar study developed a multi-organ-on-a-chip that connected three organ modules representing the liver, heart, and lung to a central fluid-routing breadboard module [104]. An electrode for measuring TEER was inserted into the lung module, and the heart module was connected to an optical camera for the real-time observation of heartbeat. Since each module was interchangeable, a combination of organ modules, rather than the connection of all three modules was possible. This modular multi-organ-on-a-chip system demonstrated that the inter-organ response significantly affected the drug response. Lai *et al* developed an interconnected 96-well plate tissue chamber that was linked through a perfusable vascular interface consisting of a supporting scaffold that defines the endothelial space and allows the self-assembly of cells into a 3D construct (liver, heart, and breast cancer) in the parenchymal space [105]. For the cardiac model, the electrodes, which were embedded in the device, could control contraction, and the cantilevers, which were embedded in the cardiac tissue, could measure the contraction. The researchers emphasized the significance of multi-organ interactions in drug screening by demonstrating a significantly different response of the breast-tumor model to a drug when connected in series to the liver construct. The chemotherapeutic drug was administered to the endothelial lumen, and its concentrations, as well as the metabolite level, were measured in the liver model. The degree of the migration of the breast-cancer cell and the drug metabolism differed in the absence and presence of the hepatic chamber. Lee *et al* developed a dual-organ-chip system that was equipped with electrochemical sensors to assess cardiotoxicity and breast-cancer progression in response to the chemotherapeutic drug (figure 6(B)) [106]. The sensors were based on a multiplexed sensing array that allows the simultaneous measurements of multiple cell-secreted biomarkers. With this platform, the effects of doxorubicin on the functionality of the iPSC-derived cardiac tissues, as well as the progression of the breast-cancer tissues (SK-BR-3 cell line), were examined by monitoring the secretion of troponin T and the production rates of the epidermal growth-factor receptor 2.

The vascular endothelium connects the organs in the body; it is essential for supporting the physiology of each organ, as well as inter-organ communication. Additionally, the tissue-to-tissue barrier between the endothelium and parenchymal cells of organs exists *in vivo*, and this barrier can substantially affect the drug response of the organs. Thus, to predict very clinically relevant pharmacokinetics, several studies introduced vascularization in multi-organ-on-a-chip systems to predict the kinetics of multiorgan interactions, as well as analyze drug efficacy and side effects on other organs [107]. For example, Herland *et al* constructed a vascularized multi-organ-on-a-chip system by grafting an automated flow system through a robot (figure 6(C)) [108]. A multi-organ-on-a-chip model was developed to separate each organ by the vascular barrier, and the organs grew in separate culture media, although they could interact through the vascular channels. This model can be used to predict and implement human pharmacokinetic responses to oral and intravenous drug administrations. To recapitulate the absorption route of orally administered drugs, the model was designed in the following order: intestine, liver, and kidney. The arteriovenous reservoir was connected to each organ to model intravenous drug administration. Additionally, an automated robotic flow device was introduced between each chip to control the speed and amount of drug spreading through the simulated organs. Through a comparative analysis of the pharmacokinetic parameters of the multi-organ-on-a-chip measured in this study with the values calculated in rodents, humans, and *in silico*, it was confirmed that the parameters of the developed platform were similar to those of actual human clinical results [109]. Ronaldson-Bouchard *et al* designed a multi-organ-on-a-chip in which each organ could be cultured in a designated optimal niche separated by a vascular barrier and flow while enabling interaction through the vasculature [110]. Four types of organs/tissues (heart, liver, bone, and skin) and endothelial cells were cultured separately before being integrated into a chip. The functional formation of the endothelial barrier was monitored by the TEER device, and the communication between the organs was confirmed *via* exosome cross-talk. This interconnected multi-organ system reflected the clinically relevant pharmacokinetic and pharmacodynamic profiles of doxorubicin and the microRNA (miRNA) biomarkers that are related to doxorubicin-induced cardiotoxicity.

5. Challenges and potential solutions

Each biosensing technology has advantages and disadvantages for the integration into organ-on-a-chip system (table 6). Electrochemical sensing modalities offer several advantages over other sensing techniques, such as low equipment setup complexity and cost-effectiveness, making them suitable for integration into microfluidic systems. These sensors allow easy miniaturization and exhibit high detection limits while requiring only small analyte volumes. However, electrochemical sensors require the frequent recalibration for their optimal long-term performance. To overcome this issue, researchers have

Table 6. Pros and cons of each biosensing technique within organ-on-a-chip.

Sensing objects	Sensing techniques	Pros	Cons
Metabolic events	Electrochemical	• High sensitivity with specific molecular bioselectivity • Relatively wide dynamic linear range and low detection limit	• Frequent recalibration for long-term monitoring • Relatively short lifespan • Sensor location should be near the cell to mitigate measurement errors
	Optical	• Non-invasive measurements • Suitable for remote monitoring	• Separate microscope systems are necessary • Interference in measurement caused by opaque obstacles • Limitation of long-term measurement due to photobleaching of the luminescent molecules
Permeability of intercellular barriers	Electrical	• Label-free sensing • Real-time monitoring with fast and high sensitivity	• Measurement values influenced by fluid flow and temperature within the chip • Precise sensor placement for achieving uniform current density
	Electrochemical	• Concurrent direct measurements while cultivating cells	• Tracer compounds may exert influence on the intracellular transport processes of cells
	Optical	• Non-invasive measurements • Suitable for remote monitoring	• Moderate sensitivity to detect subtle changes in transmittance • Separate microscope systems are necessary • Interference in measurement caused by opaque obstacles • Limitation of long-term measurement due to photobleaching of the luminescent molecules
Biological signals	Electrical signals (MEA)	• Detection of electrical signals from diverse spatial locations • Capturing complex network interactions and synchronized activity patterns among cells	• Limitations in capturing complex 3D spatial interactions and dynamics within cellular networks • Limitation to selection of sensor materials • Challenging to implementing spatial resolution comparable to patch-clamp techniques
	Physical signals (cantilever)	• Label-free and non-destructive measurements • Real-time measurement of mechanical movements at the 3D tissue level	• Limited spatial resolution to measure changes at the individual cells • Optical imaging-based analysis affects the equipment's resolution
Others	Omics analysis	• Acquisition and analysis of a multitude of biological information	• Limitation of continuous monitoring as the cultivation should be stopped • High-cost implications for conducting high-throughput research
	Multi-sensing	• Analyze comprehensive biological information	• Complexity of the interface poses challenges for user accessibility • Signal interference among analysis equipment

focused on sensor calibration automation. A notable example is the work by Giménez-Gómez *et al* [111], which designed a self-recalibrating lab-on-a-chip. Their biosensor incorporated four independent micro-electrodes capable of detecting glucose, hydrogen peroxide, conductivity, and oxidation reduction potential, allowing the analysis of oxidative stress. Importantly, this system could reactivate and recalibrate the electrochemical electrodes without compromising cell viability. In another study led by Bavli *et al* [35], a liver-on-a-chip device integrated sensors in an external unit, which allowed the experiment to continue even if the chip device requires replacement, as the sensing component remained separate from the organ-on-a-chip. Moreover, the off-chip setup facilitated automated sensor calibration and the generation of precise chemical gradients to ensure measurement stability.

Optical biosensors offer real-time analysis of various analytes with high temporal resolution [112]. Optical biosensors based on surface plasmon resonance, total internal reflection-based sensors, photonic crystals, ring resonators, and waveguide fibers have been used for label-free detection methods. However, ambient light and inhomogeneities in the illumination field interfere with analytical signals, and the long-term stability is also limited due to bleaching of the indicators. Various strategies have been developed to improve the signal-to-noise ratio and lifetime of the indicators [113]. These strategies involve optimizing the substrate materials, their structural properties, and integration with supplementary materials [114, 115]. Additionally, selecting the appropriate wavelength of the incident light is critical in enhancing the sensitivity of optical sensors. Chemical signal amplification has also been suggested to be an effective strategy to enhance the sensitivity of optical biosensors. One approach is to use micro- or nanocarriers loaded with multiple signaling molecules as probes, thus increasing the number or intensity of signals per event [116]. Another method involves utilizing different signal modalities, such as near-infrared-emitting fluorophores or plasmon-enhanced fluorescence, to improve the signal-to-noise ratio [117, 118]. Chemical reactions can also be introduced at the signal-transducing step to amplify the signals [119]. Polymerization-based signal amplification is achieved through the controlled growth of polymers from initiators conjugated to biomolecules, enabling target-triggered polymerization. Inorganic metal-based nanocatalysts can replace enzymes for catalytic amplification of signals [120].

The integration of a TEER measurement system within an organ-on-a-chip enables continuous and non-invasive monitoring of cells without disrupting the cell culture environment. However, the presence of electrodes poses challenges by restricting the field of view, thereby limiting access to the cells during imaging. Additionally, precise TEER measurements are contingent upon various factors such as electrode materials, properties, positioning, uniformity of current density across the cellular monolayer, and the electrical circuit model used for data interpretation [121]. TEER measurements are also susceptible to the influence of factors, including temperature and electrolyte concentrations [122]. Scale-down of electrode size is inevitable for integration of electrodes into the organ-on-a-chip, which causes a non-uniform field across the chip due to relatively small size to the cultured region, ultimately leading to unreliable impedance data. To address this issue, thinner layers of metal can be deposited to achieve a current density distribution that involves the entire cell culture area, while still allowing optical inspection [123]. However, these semitransparent electrodes exhibit high electrode polarization impedance, which filters out signal content below the electrode cutoff frequency. Among various electrode materials proposed for TEER measurement, one promising alternative is the organic semiconductor polymer (PEDOT:PSS) [124]. PEDOT:PSS has shown improved recording performance for opaque electrodes in impedance measurements, as it is less affected by electrode polarization impedance compared to inorganic materials. Additionally, PEDOT:PSS offers a favorable compromise between electrical properties and transparency, making it suitable for simultaneous electrical activity recording and optical imaging. A recent study successfully utilized PEDOT:PSS to monitor the impedance of cellular barriers while enabling optical inspection in an organ-on-a-chip [125]. In this work, an organ-on-a-chip device with integrated semitransparent PEDOT:PSS electrodes was developed to monitor intestinal barrier tissue function, overcoming the limitations of current EIS setups in organ-on-a-chip systems. The homogeneous current distribution provided by PEDOT:PSS electrodes covering the entire cell culture area ensured equal contribution from the entire culture region in the chip to the measured impedance. Finally, the application of TEER is complicated for epithelial culture that require an air–liquid interface, as the model needs to be completely submerged in the culture medium to ensure electrical connection. To solve this problem, Mermoud *et al* developed a micro-impedance tomography system integrated in a lung-on-a-chip to monitor the resistivity changes and movements of the lung alveolar barrier [59].

The performance of biosensors in organ-on-a-chip can be improved by using nanomaterials (*e.g.* gold nanoparticles, carbon nanotubes, *etc*) [126]. Engineered nanomaterials offer several advantages, such as higher electrical conductivity, increased surface-to-volume ratio, chemical activity, mechanical strength, electrocatalytic properties, and enhanced diffusivity. These properties significantly

improve the sensitivity and lower the limit of detection of biosensors. Increasing the surface area available for binding to target molecules is a common strategy for signal amplification in biosensors. Nanomaterials with high surface-to-volume ratios, such as gold nanoparticles and carbon nanotubes, are frequently employed for this purpose as they provide a larger binding interface, allowing them to bind to a greater number of target molecules and thereby amplify the signals in bioassays. Nanomaterials can also act as scaffolds for immobilizing biomolecules. This can be achieved by functionalizing the surface of the nanomaterials with specific chemical groups that enable the immobilization of biomolecules (*e.g.* enzymes, antibodies) in a specific orientation, leading to the increase in the efficiency of the bioassay and the generated signals.

Nanomaterials can facilitate signal amplification by acting as electrochemical or optical transducers. For instance, in a previous study to integrate TEER sensors and electrochemical sensors into a gut-on-a-chip system to monitor cell barrier integrity and the absorption of Mercury (Hg(II)) [127], gold nanoparticles were used to coat the electrodes and detect Hg(II) absorption by intestinal epithelial cells based on the principle of the redox reaction. Gold nanomaterials could also be employed for enhancing the detection of target molecules (*e.g.* miRNA) using surface-enhanced Raman spectroscopy [128]. Another study demonstrated a plasmonic biosensing platform that utilizes a commercially available optical disc with polymeric templates containing nanograting [129]. The bare polymeric nanograting was coated with a thin, optimized layer of gold and then the nanograting surface was immobilized with IL-6 and insulin antibodies. This plasmonic biosensor was integrated into a chamber-type organ-on-a-chip platform with co-culture of skeletal muscle cells (C2C12) and pancreatic islet cells (MIN6 cell line) to monitor the real-time secretion of IL-6 by skeletal muscle cells in response to electrical stimulation and investigate its effect on stimulating insulin production in pancreatic islet cells. Although graphene and quantum dots have been rarely utilized for sensor materials for organ-on-a-chip models, they would be able to offer high sensitivity and specificity for detecting target molecules in organ-on-a-chip owing to their unique electrochemical and optical properties [130–132]. In summary, nanomaterials offer a wide range of advantages and functionalities that can significantly enhance the performance of biosensors in organ-on-a-chip systems, leading to improved accuracy and sensitivity in biosensing applications.

The integration of machine learning presents significant potential for advancing organ-on-a-chip models. Machine learning techniques find valuable applications in target recognition, segmentation, reconstruction, and detection. For image processing, techniques like segmentation and super-resolution reconstruction enhance image quality and analysis. Automatic data annotation algorithms efficiently label large amounts of unlabeled data, improving prediction accuracy in cell networks for tasks like classifying single-cell trajectories, tracking cells, and analyzing motion in time-lapse microscopy images. For instance, Biselli *et al* employed machine learning algorithms to reconstruct a tumor-on-a-chip model *via* co-culture of peripheral blood mononuclear cells with $HER2^+$ tumor cells, allowing accurate cell tracking during time-lapse microscopy experiments [133]. Mencattini *et al* achieved successful classification of single-cell trajectories of peripheral blood mononuclear cells and cancer cells based on the presence or absence of a drug [134]. This study involved analyzing cell motility behaviors of peripheral blood mononuclear cells co-cultured with $HER2^+$ breast cancer cells (BT474 cell line) in an organ-on-a-chip system, using time-lapse microscopy images. Single-cell trajectories were collected and a pre-trained deep learning convolutional neural network architecture was employed to extract relevant features for classification tasks from this visual atlas. Deep learning integration in organ-on-a-chip systems enables visualization and quantification of complex dynamics within the tumor microenvironment, as demonstrated by Nguyen *et al* [135]. The development of deep learning tools, such as deep tracking, allows for improved accuracy in analyzing cell trajectories and understanding cell interactions. Jena *et al* applied machine learning techniques, including recurrent neural networks and convolutional neural networks, to generate a human muscle-on-a-chip model, which facilitates the determination of biochemical markers and providing insights into muscle cell physiology [136].

Machine learning algorithms play a crucial role in analyzing vast amounts of data produced from multiple sensing modalities in organ-on-a-chip models. These algorithms have the capability to integrate and fuse diverse datasets, thereby facilitating a comprehensive understanding of the system and enabling the identification of intricate relationships between various variables. By detecting patterns, correlations, and anomalies within the data, machine learning algorithms extract meaningful information and offer valuable insights into cellular behavior, tissue function, and drug responses. In the context of a human-on-a-chip, which encompasses multiple tissues, deep learning methodologies would provide valuable tools to analyze the multi-scale data from each tissue and their interactions.

Deep learning can also be applied to device design, material selection, and fluidic modeling, enabling effective prediction. Machine learning models can suggest optimized device designs, including channel geometries, microstructures, and surface coatings, thereby improving the functionality

of organ-on-a-chip platforms [137]. Furthermore, machine learning enables the development of predictive models for fluidic behavior within organ-on-a-chip devices. By analyzing experimental data on fluid flow rates, pressure drops, and cell responses, machine learning algorithms can discern underlying relationships among the variables and construct the models that predict fluidic behavior under different conditions. This capability empowers researchers to optimize flow parameters, design more efficient microfluidic networks, and anticipate how variations in flow can impact cellular responses.

6. Conclusion

A conventional 2D culture allows the analysis of the degree of cell response in a particular environment, but the 2D culture is not appropriate for modeling precise organ response, hence the continuous attempts to simulate and construct organs. One method for achieving this involves mimicking the *in vivo* organ environment in an organ-on-a-chip as closely as possible to induce a more realistic response. In this review, we described state-of-the-art studies that combined organ-on-a-chip technologies and sensing systems for monitoring different relevant biological information (*e.g.* metabolite level, membrane permeability, electrical signals, and enzyme activity). Over the past decade, significant improvements have been made in organ-on-a-chip models coupled with biosensors regarding their complexity, quality, and robustness. While different types of biosensors have been developed as on-chip monitoring systems, there is still potential for further improvement in several areas.

All types of the biosensors for integration into organ-on-a-chip system encounter common challenges such as the complexity increased by sensor integration to microfluidic platform and cost issue. In addition, an increase in cellular and environmental complexity of organ-on-a-chip system for physiological relevance to human organs and tissues results in the operational complexity, limited coordination, and scalability of the biosensors. Finally, the large size and structural complexity of 3D constructs and organoids in the organ-on-a-chip system are also likely to present challenges to imaging, monitoring, and analysis, which could be tackled by developing advanced 3D imaging techniques and probes tailored to such organ-like constructs.

In parallel, recent initiatives have advanced sensor-integrated organ-on-a-chip technology to the next level by combining multi-sensing and multi-organ-on-a-chip technologies to simulate the entire biological process, and this can ensure the accurate modeling of pharmacokinetic profiles for drug assessment, as well as the monitoring of multiparametric biomarkers. However, these technologies are still in their infancy, a lot is still required before they can be fully deployed as substitutes for animal models. To generate reliable data in such complex platforms, it is necessary to build a systematic and coordinated linkage system between *in vitro* organ-chip models, such as a vasculature with blood flow, and reduce the interference between multiple sensors. Additionally, the standardization of the organ culture, as well as the validation of cellular measurements *via* correlation analysis employing the clinical data, must be further investigated. As a next step, the establishment of reliable HTS chip platforms along with real-time HCS methods, as well as on-chip omics analysis, may advance organ-on-a-chip technology. Further, advanced biosensing technologies, such as the pharmacokinetics and pharmacological profile analyses of specific drugs and disease-related biomarker measurements, must be applied to multi-organ-on-a-chip technologies that mimic human physiology by combining multiple organ chips.

The integration of commercially available organ-on-a-chip systems with biosensors shows promising potential for more accurate and efficient preclinical drug testing, disease modeling, and personalized medicine applications. Several examples of such integrated systems exist, including the 'OrganoPlate®' of Mimetas, a microfluidic platform that enables the culture of multiple cell types in a 3D matrix, integrated with biosensors for real-time monitoring of TEER. Another noteworthy system is the 'Human-on-a-chip®' developed by Hesperos Inc., a multi-organ microfluidic setup incorporating MEA and TEER to monitor electrical activity and barrier integrity changes, respectively. TissUse GmbH has introduced the 'HUMIMIC ActSense', a versatile device capable of measuring TEER, performing impedance spectroscopy, sensing high-resolution electrical activity, and stimulating electrically-active tissue, all within a single platform [138]. This platform has been applied to study intestinal diseases and assess the absorption and toxicity of orally administered drugs. Additionally, Elveflow is currently in the process of developing a lung-on-a-chip platform that can be seamlessly integrated with various sensors, including microfluidic flow and pressure sensors. Despite the promising outlook, several challenges must be addressed to successfully commercialize organ-on-a-chip integrated sensor platforms. Challenges remain in terms of scalability, cost-effectiveness, regulatory compliance, safety, and efficacy assessments. Long-term stability, sensor calibration, and data interpretation also require ongoing research and further development. Collaborative efforts among researchers, industry stakeholders, and regulatory bodies are necessary to establish standards and guidelines for validation, qualification, and translation.

Data availability statement

No new data were created or analysed in this study.

Acknowledgments

This work was supported by the Samsung Research Funding & Incubation Center of Samsung Electronics (SRFC-TC2003-03). This work was also supported by Yonsei Signature Research Cluster Program (2023-22-0012) and Yonsei Fellow Program funded by Lee Youn Jae.

ORCID iDs

Yoonhee Jin https://orcid.org/0000-0002-1263-9405
Seung-Woo Cho https://orcid.org/0000-0001-8058-332X

References

[1] Kavand H, Nasiri R and Herland A 2022 Advanced materials and sensors for microphysiological systems: focus on electronic and electrooptical interfaces *Adv. Mater.* **34** e2107876
[2] Shah P *et al* 2016 A microfluidics-based *in vitro* model of the gastrointestinal human–microbe interface *Nat. Commun.* **7** 1–15
[3] Yang K, Han S, Shin Y, Ko E, Kim J, Park K I, Chung S and Cho S-W 2013 A microfluidic array for quantitative analysis of human neural stem cell self-renewal and differentiation in three-dimensional hypoxic microenvironment *Biomaterials* **34** 6607–14
[4] Yang K *et al* 2015 Recapitulation of in vivo-like paracrine signals of human mesenchymal stem cells for functional neuronal differentiation of human neural stem cells in a 3D microfluidic system *Biomaterials* **63** 177–88
[5] Zhang K, Feng Q, Fang Z, Gu L and Bian L 2021 Structurally dynamic hydrogels for biomedical applications: pursuing a fine balance between macroscopic stability and microscopic dynamics *Chem. Rev.* **121** 11149–93
[6] Han S, Yang K, Shin Y, Lee J S, Kamm R D, Chung S and Cho S-W 2012 Three-dimensional extracellular matrix-mediated neural stem cell differentiation in a microfluidic device *Lab Chip* **12** 2305–8
[7] Park S E, Georgescu A and Huh D 2019 Organoids-on-a-chip *Science* **364** 960–5
[8] Polacheck W J, Li R, Uzel S G M and Kamm R 2013 Microfluidic platforms for mechanobiology *Lab Chip* **13** 2252–67
[9] Shin Y, Yang K, Han S, Park H-J, Seok Heo Y, Cho S-W and Chung S 2014 Reconstituting vascular microenvironment of neural stem cell niche in three-dimensional extracellular matrix *Adv. Healthcare Mater.* **3** 1457–64
[10] Fritschen A and Blaeser A 2021 Biosynthetic, biomimetic, and self-assembled vascularized organ-on-a-chip systems *Biomaterials* **268** 120556
[11] Luttge R 2022 Nanofabricating neural networks: strategies, advances, and challenges *J. Vac. Sci. Technol.* B **40** 020801
[12] Marrero D, Pujol-Vila F, Vera D, Gabriel G, Illa X, Elizalde-Torrent A, Alvarez M and Villa R 2021 Gut-on-a-chip: mimicking and monitoring the human intestine *Biosens. Bioelectron.* **181** 113156
[13] Valverde M G, Mille L S, Figler K P, Cervantes E, Li V Y, Bonventre J V, Masereeuw R and Zhang Y S 2022 Biomimetic models of the glomerulus *Nat. Rev. Nephrol.* **18** 241–57
[14] Wang J, Khodabukus A, Rao L, Vandusen K, Abutaleb N and Bursac N 2019 Engineered skeletal muscles for disease modeling and drug discovery *Biomaterials* **221** 119416
[15] Cho A-N *et al* 2021 Microfluidic device with brain extracellular matrix promotes structural and functional maturation of human brain organoids *Nat. Commun.* **12** 1–23
[16] Hofer M and Lutolf M P 2021 Engineering organoids *Nat. Rev. Mater.* **6** 402–20
[17] Jin Y, Kim J, Lee J S, Min S, Kim S, Ahn D-H, Kim Y-G and Cho S-W 2018 Vascularized liver organoids generated using induced hepatic tissue and dynamic liver-specific microenvironment as a drug testing platform *Adv. Funct. Mater.* **28** 1801954
[18] Kim J, Koo B-K and Knoblich J A 2020 Human organoids: model systems for human biology and medicine *Nat. Rev. Mol. Cell. Biol.* **21** 571–84
[19] Lancaster M A and Knoblich J A 2014 Organogenesis in a dish: modeling development and disease using organoid technologies *Science* **345** 1247125
[20] Modena M M, Chawla K, Misun P M and Hierlemann A 2018 Smart cell culture systems: integration of sensors and actuators into microphysiological systems *ACS Chem. Biol.* **13** 1767–84
[21] Riahi R, Shaegh S A M, Ghaderi M, Zhang Y S, Shin S R, Aleman J, Massa S, Kim D, Dokmeci M R and Khademhosseini A 2016 Automated microfluidic platform of bead-based electrochemical immunosensor integrated with bioreactor for continual monitoring of cell secreted biomarkers *Sci. Rep.* **6** 1–14
[22] Fuchs S, Johansson S, Tjell A Ø, Werr G, Mayr T and Tenje M 2021 In-line analysis of organ-on-chip systems with sensors: integration, fabrication, challenges, and potential *ACS Biomater. Sci. Eng.* **7** 2926–48
[23] Santbergen M J C, van der Zande M, Bouwmeester H and Nielen M W F 2019 Online and *in situ* analysis of organs-on-a-chip *Trends Analyt. Chem.* **115** 138–46
[24] Young A T, Rivera K R, Erb P D and Daniele M A 2019 Monitoring of microphysiological systems: integrating sensors and real-time data analysis toward autonomous decision-making *ACS Sens.* **4** 1454–64
[25] Zhu Y *et al* 2021 State of the art in integrated biosensors for organ-on-a-chip applications *Curr. Opin. Biomed. Eng.* **19** 100309
[26] Vunjak-Novakovic G, Ronaldson-Bouchard K and Radisic M 2021 Organs-on-a-chip models for biological research *Cell* **184** 4597–611
[27] Zarrintaj P, Saeb M R, Stadler F J, Yazdi M K, Nezhad M N, Mohebbi S, Seidi F, Ganjali M R and Mozafari M 2022 Human organs-on-chips: a review of the state-of-the-art, current prospects, and future challenges *Adv. Biol.* **6** e2000526
[28] Weltin A, Hammer S, Noor F, Kaminski Y, Kieninger J and Urban G A 2017 Accessing 3D microtissue metabolism: lactate and oxygen monitoring in hepatocyte spheroids *Biosens. Bioelectron.* **87** 941–8
[29] Moya A, Ortega-Ribera M, Guimerà X, Sowade E, Zea M, Illa X, Ramon E, Villa R, Gracia-Sancho J and Gabriel G 2018 Online oxygen monitoring using integrated inkjet-printed sensors in a liver-on-a-chip system *Lab Chip* **18** 2023–35
[30] Dornhof J, Kieninger J, Muralidharan H, Maurer J, Urban G A and Weltin A 2022 Microfluidic organ-on-chip system for multi-analyte monitoring of metabolites in 3D cell cultures *Lab Chip* **22** 225–39
[31] Ortega M A, Fernández-Garibay X, Castaño A G, De Chiara F, Hernández-Albors A, Balaguer-Trias J and Ramón-Azcón J 2019 Muscle-on-a-chip with an on-site multiplexed biosensing system for *in situ* monitoring of secreted IL-6 and TNF-α *Lab Chip* **19** 2568–80

[32] Gao B, Liao J, Guo M, Liu H, He B and Gu Z 2019 Biomimetic meta-structured electro-microfluidics *Adv. Funct. Mater.* **29** 1906745
[33] Shang W, Chen C-Y, Lo K, Payne G F and Bentley W E 2019 Chip modularity enables molecular information access from organ-on-chip devices with quality control *Sens. Actuators* B **295** 30–39
[34] Lee M-H, Thomas J L, Su Z-L, Yeh W-K, Monzel A S, Bolognin S, Schwamborn J C, Yang C-H and Lin H-Y 2021 Epitope imprinting of alpha-synuclein for sensing in Parkinson's brain organoid culture medium *Biosens. Bioelectron.* **175** 112852
[35] Bavli D, Prill S, Ezra E, Levy G, Cohen M, Vinken M, Vanfleteren J, Jaeger M and Nahmias Y 2016 Real-time monitoring of metabolic function in liver-on-chip microdevices tracks the dynamics of mitochondrial dysfunction *Proc. Natl Acad. Sci. USA* **113** E2231–40
[36] Müller B, Sulzer P, Walch M, Zirath H, Buryška T, Rothbauer M, Ertl P and Mayr T 2021 Measurement of respiration and acidification rates of mammalian cells in thermoplastic microfluidic devices *Sens. Actuators* B **334** 129664
[37] McCracken K W, Aihara E, Martin B, Crawford C M, Broda T, Treguier J, Zhang X, Shannon J M, Montrose M H and Wells J M 2017 Wnt/β-catenin promotes gastric fundus specification in mice and humans *Nature* **541** 182–7
[38] Matsumoto S, Leclerc E, Maekawa T, Kinoshita H, Shinohara M, Komori K, Sakai Y and Fujii T 2018 Integration of an oxygen sensor into a polydymethylsiloxane hepatic culture device for two-dimensional gradient characterization *Sens. Actuators* B **273** 1062–9
[39] Zirath H *et al* 2018 Every breath you take: non-invasive real-time oxygen biosensing in two- and three-dimensional microfluidic cell models *Front. Physiol.* **9** 815
[40] Wang C, Dang T, Baste J, Anil Joshi A and Bhushan A 2021 A novel standalone microfluidic device for local control of oxygen tension for intestinal-bacteria interactions *FASEB J.* **35** e21291
[41] Grant J, Lee E, Almeida M, Kim S, LoGrande N, Goyal G, Sesay A M, Breault D T, Prantil-Baun R and Ingber D E 2022 Establishment of physiologically relevant oxygen gradients in microfluidic organ chips *Lab Chip* **22** 1584–93
[42] Cognetti J S, Moen M T, Brewer M G, Bryan M R, Tice J D, McGrath J L and Miller B L 2023 A photonic biosensor-integrated tissue chip platform for real-time sensing of lung epithelial inflammatory markers *Lab Chip* **23** 239–50
[43] Jalili-Firoozinezhad S *et al* 2019 A complex human gut microbiome cultured in an anaerobic intestine-on-a-chip *Nat. Biomed. Eng.* **3** 520–31
[44] Rogal J, Binder C, Kromidas E, Roosz J, Probst C, Schneider S, Schenke-Layland K and Loskill P 2020 WAT-on-a-chip integrating human mature white adipocytes for mechanistic research and pharmaceutical applications *Sci. Rep.* **10** 6666
[45] Rizzuto V, Mencattini A, Álvarez-González B, Di Giuseppe D, Martinelli E, Beneitez-Pastor D, Mañú-Pereira M D M, Lopez-Martinez M J and Samitier J 2021 Combining microfluidics with machine learning algorithms for RBC classification in rare hereditary hemolytic anemia *Sci. Rep.* **11** 13553
[46] Liang Y and Yoon J-Y 2021 *In situ* sensors for blood-brain barrier (BBB) on a chip *Sens. Actuators Rep.* **3** 100031
[47] Franco R and Cedazo-Minguez A 2014 Successful therapies for Alzheimer's disease: why so many in animal models and none in humans? *Front. Pharmacol.* **5** 146
[48] Oddo A, Peng B, Tong Z, Wei Y, Tong W Y, Thissen H and Voelcker N H 2019 Advances in microfluidic blood–brain barrier (BBB) models *Trends Biotechnol.* **37** 1295–314
[49] Peterson L W and Artis D 2014 Intestinal epithelial cells: regulators of barrier function and immune homeostasis *Nat. Rev. Immunol.* **14** 141–53
[50] Wiesner D L and Klein B S 2017 Lung epithelium: barrier immunity to inhaled fungi and driver of fungal-associated allergic asthma *Curr. Opin. Microbiol.* **40** 8–13
[51] Henry O Y F, Villenave R, Cronce M J, Leineweber W D, Benz M A and Ingber D E 2017 Organs-on-chips with integrated electrodes for trans-epithelial electrical resistance (TEER) measurements of human epithelial barrier function *Lab Chip* **17** 2264–71
[52] Stucki J D *et al* 2018 Medium throughput breathing human primary cell alveolus-on-chip model *Sci. Rep.* **8** 14359
[53] Yeste J, García-Ramírez M, Illa X, Guimerà A, Hernández C, Simó R and Villa R 2018 A compartmentalized microfluidic chip with crisscross microgrooves and electrophysiological electrodes for modeling the blood–retinal barrier *Lab Chip* **18** 95–105
[54] Schuller P *et al* 2020 A lab-on-a-chip system with an embedded porous membrane-based impedance biosensor array for nanoparticle risk assessment on placental Bewo trophoblast cells *Sens. Actuators* B **312** 127946
[55] Choudhury M I *et al* 2022 Kidney epithelial cells are active mechano-biological fluid pumps *Nat. Commun.* **13** 2317
[56] Salih A R C, Farooqi H M U, Kim Y S, Lee S H and Choi K H 2020 Impact of serum concentration in cell culture media on tight junction proteins within a multiorgan microphysiological system *Microelectron. Eng.* **232** 111405
[57] Amiri P, DeCastro J, Littig J, Lu H-W, Liu C, Conboy I and Aran K 2021 Erythrocytes, a new contributor to age-associated loss of blood-brain barrier integrity *Adv. Sci.* **8** e2101912
[58] Renous N, Kiri M D, Barnea R A, Rauti R, Leichtmann-Bardoogo Y and Maoz B M 2021 Spatial trans-epithelial electrical resistance (S-TEER) integrated in organs-on-chips *Lab Chip* **22** 71–79
[59] Mermoud Y, Felder M, Stucki J D, Stucki A O and Guenat O T 2018 Microimpedance tomography system to monitor cell activity and membrane movements in a breathing lung-on-chip *Sens. Actuators* B **255** 3647–53
[60] Moysidou C-M, Pitsalidis C, Al-Sharabi M, Withers A M, Zeitler J A and Owens R M 2021 3D bioelectronic model of the human intestine *Adv. Biol.* **5** 2000306
[61] Nashimoto Y, Abe M, Fujii R, Taira N, Ida H, Takahashi Y, Ino K, Ramon-Azcon J and Shiku H 2021 Topography and permeability analyses of vasculature-on-a-chip using scanning probe microscopies *Adv. Healthcare Mater.* **10** 2101186
[62] Wong J F and Simmons C A 2019 Microfluidic assay for the on-chip electrochemical measurement of cell monolayer permeability *Lab Chip* **19** 1060–70
[63] Wong J F, Mohan M D, Young E W K and Simmons C A 2020 Integrated electrochemical measurement of endothelial permeability in a 3D hydrogel-based microfluidic vascular model *Biosens. Bioelectron.* **147** 111757
[64] Ino K, Pai H-J, Hiramoto K, Utagawa Y, Nashimoto Y and Shiku H 2021 Electrochemical imaging of endothelial permeability using a large-scale integration-based device *ACS Omega* **6** 35476–83
[65] Partyka P P, Godsey G A, Galie J R, Kosciuk M C, Acharya N K, Nagele R G and Galie P A 2017 Mechanical stress regulates transport in a compliant 3D model of the blood-brain barrier *Biomaterials* **115** 30–39
[66] Lai B F L, Lu R X Z, Hu Y, Davenport Huyer L, Dou W, Wang E Y, Radulovich N, Tsao M S, Sun Y and Radisic M 2020 Recapitulating pancreatic tumor microenvironment through synergistic use of patient organoids and organ-on-a-chip vasculature *Adv. Funct. Mater.* **30** 2000545
[67] Carvalho M, Barata D, Teixeira L M, Giselbrecht S, Reis R L, Oliveira J M, Truckenmüller R and Habibovic P 2019 Colorectal tumor-on-a-chip system: a 3D tool for precision onco-nanomedicine *Sci. Adv.* **5** eaaw1317
[68] Feiner-Gracia N, Glinkowska Mares A, Buzhor M, Rodriguez-Trujillo R, Samitier Marti J, Amir R J, Pujals S

and Albertazzi L 2021 Real-time ratiometric imaging of micelles assembly state in a microfluidic cancer-on-a-chip *ACS Appl. Biol. Mater.* **4** 669–81
[69] Mollica H, Palomba R, Primavera R and Decuzzi P 2019 Two-channel compartmentalized microfluidic chip for real-time monitoring of the metastatic cascade *ACS Biomater. Sci. Eng.* **5** 4834–43
[70] Kim J *et al* 2021 Fungal brain infection modelled in a human-neurovascular-unit-on-a-chip with a functional blood–brain barrier *Nat. Biomed. Eng.* **5** 830–46
[71] Moutaux E, Charlot B, Genoux A, Saudou F and Cazorla M 2018 An integrated microfluidic/microelectrode array for the study of activity-dependent intracellular dynamics in neuronal networks *Lab Chip* **18** 3425–35
[72] Ao Z, Cai H, Wu Z, Krzesniak J, Tian C, Lai Y Y, Mackie K and Guo F 2021 Human spinal organoid-on-a-chip to model nociceptive circuitry for pain therapeutics discovery *Anal. Chem.* **94** 1365–72
[73] Zhang F, Cheng H, Qu K, Qian X, Lin Y, Zhang Y, Qian S, Huang N, Cui C and Chen M 2023 Continuous contractile force and electrical signal recordings of 3D cardiac tissue utilizing conductive hydrogel pillars on a chip *Mater. Today Bio* **20** 100626
[74] Visone R, Ugolini G S, Cruz-Moreira D, Marzorati S, Piazza S, Pesenti E, Redaelli A, Moretti M, Occhetta P and Rasponi M 2021 Micro-electrode channel guide (microECG) technology: an online method for continuous electrical recording in a human beating heart-on-chip *Biofabrication* **13** 035026
[75] Liu H, Bolonduro O A, Hu N, Ju J, Rao A A, Duffy B M, Huang Z, Black L D and Timko B P 2020 Heart-on-a-chip model with integrated extra- and intracellular bioelectronics for monitoring cardiac electrophysiology under acute hypoxia *Nano Lett.* **20** 2585–93
[76] Park Y *et al* 2021 Three-dimensional, multifunctional neural interfaces for cortical spheroids and engineered assembloids *Sci. Adv.* **7** eabf9153
[77] Kalmykov A *et al* 2019 Organ-on-e-chip: three-dimensional self-rolled biosensor array for electrical interrogations of human electrogenic spheroids *Sci. Adv.* **5** eaax0729
[78] Li Q, Nan K, Le Floch P, Lin Z, Sheng H, Blum T S and Liu J 2019 Cyborg organoids: implantation of nanoelectronics via organogenesis for tissue-wide electrophysiology *Nano Lett.* **19** 5781–9
[79] Le Floch P, Li Q, Lin Z, Zhao S, Liu R, Tasnim K, Jiang H and Liu J 2022 Stretchable mesh nanoelectronics for 3D single-cell chronic electrophysiology from developing brain organoids *Adv. Mater.* **34** 2106829
[80] Uzel S G, Platt R J, Subramanian V, Pearl T M, Rowlands C J, Chan V, Boyer L A, So P T C and Kamm R D 2016 Microfluidic device for the formation of optically excitable, three-dimensional, compartmentalized motor units *Sci. Adv.* **2** e1501429
[81] Osaki T, Uzel S G and Kamm R D 2018 Microphysiological 3D model of amyotrophic lateral sclerosis (ALS) from human iPS-derived muscle cells and optogenetic motor neurons *Sci. Adv.* **4** eaat5847
[82] Chen Y, Chan H N, Michael S A, Shen Y, Chen Y, Tian Q, Huang L and Wu H 2017 A microfluidic circulatory system integrated with capillary-assisted pressure sensors *Lab Chip* **17** 653–62
[83] Nelson M R, Ghoshal D, Mejías J C, Rubio D F, Keith E and Roy K 2021 A multi-niche microvascularized human bone marrow (hBM) on-a-chip elucidates key roles of the endosteal niche in hBM physiology *Biomaterials* **270** 120683
[84] Lee S, Kang H, Park D, Yu J, Koh S K, Cho D, Kim D-H, Kang K-S and Jeon N L 2021 Modeling 3D human tumor lymphatic vessel network using high-throughput platform *Adv. Biol.* **5** 2000195
[85] Nicolas A *et al* 2021 High throughput transepithelial electrical resistance (TEER) measurements on perfused membrane-free epithelia *Lab Chip* **21** 1676–85
[86] Paek K, Kim S, Tak S, Kim M K, Park J, Chung S, Park T H and Kim J A 2022 A high-throughput biomimetic bone-on-a-chip platform with artificial intelligence-assisted image analysis for osteoporosis drug testing *Bioeng. Transl. Med.* **8** e10313
[87] Tovaglieri A *et al* 2019 Species-specific enhancement of enterohemorrhagic E. coli pathogenesis mediated by microbiome metabolites *Microbiome* **7** 1–21
[88] Wiedenmann S *et al* 2021 Single-cell-resolved differentiation of human induced pluripotent stem cells into pancreatic duct-like organoids on a microwell chip *Nat. Biomed. Eng.* **5** 897–913
[89] Si L *et al* 2021 A human-airway-on-a-chip for the rapid identification of candidate antiviral therapeutics and prophylactics *Nat. Biomed. Eng.* **5** 815–29
[90] Shaughnessey E M, Kann S H, Azizgolshani H, Black L D, Charest J L and Vedula E M 2022 Evaluation of rapid transepithelial electrical resistance (TEER) measurement as a metric of kidney toxicity in a high-throughput microfluidic culture system *Sci. Rep.* **12** 13182
[91] Maoz B M *et al* 2017 Organs-on-chips with combined multi-electrode array and transepithelial electrical resistance measurement capabilities *Lab Chip* **17** 2294–302
[92] Zhang Y S *et al* 2017 Multisensor-integrated organs-on-chips platform for automated and continual *in situ* monitoring of organoid behaviors *Proc. Natl Acad. Sci. USA* **114** E2293–302
[93] Farooqi H M U, Khalid M A U, Kim K H, Lee S R and Choi K H 2020 Real-time physiological sensor-based liver-on-chip device for monitoring drug toxicity *J. Micromech. Microeng.* **30** 115013
[94] Asif A, Kim K H, Jabbar F, Kim S and Choi K H 2020 Real-time sensors for live monitoring of disease and drug analysis in microfluidic model of proximal tubule *Microfluid Nanofluidics* **24** 1–10
[95] Azizgolshani H *et al* 2021 High-throughput organ-on-chip platform with integrated programmable fluid flow and real-time sensing for complex tissue models in drug development workflows *Lab Chip* **21** 1454–74
[96] Oleaga C *et al* 2016 Multi-organ toxicity demonstration in a functional human *in vitro* system composed of four organs *Sci. Rep.* **6** 1–17
[97] Carvalho C, Santos R, Cardoso S, Correia S, Oliveira P, Santos M and Moreira P 2009 Doxorubicin: the good, the bad and the ugly effect *Curr. Med. Chem* **16** 3267–85
[98] Duenas-Gonzalez A, Candelaria M, Perez-Plascencia C, Perez-Cardenas E, de la Cruz-hernandez E and Herrera L A 2008 Valproic acid as epigenetic cancer drug: preclinical, clinical and transcriptional effects on solid tumors *Cancer Treat. Rev.* **34** 206–22
[99] Hadzimichalis N M, Baliga S S, Golfetti R, Jaques K M, Firestein B L and Merrill G F 2007 Acetaminophen-mediated cardioprotection via inhibition of the mitochondrial permeability transition pore-induced apoptotic pathway *Am. J. Physiol. Heart Circ. Physiol.* **293** H3348–55
[100] Lins R L, Matthys K E, Verpooten G A, Peeters P C, Dratwa M, Stolear J-C and Lameire N H 2003 Pharmacokinetics of atorvastatin and its metabolites after single and multiple dosing in hypercholesterolaemic haemodialysis patients *Nephrol. Dial. Transplant.* **18** 967–76
[101] Löscher W 2002 Basic pharmacology of valproate *CNS Drugs* **16** 669–94
[102] Skottheim I B, Gedde-Dahl A, Hejazifar S, Hoel K and Åsberg A 2008 Statin induced myotoxicity: the lactone forms are more potent than the acid forms in human skeletal muscle cells *in vitro Eur. J. Pharm. Sci.* **33** 317–25
[103] Oleaga C *et al* 2019 Long-term electrical and mechanical function monitoring of a human-on-a-chip system *Adv. Funct .Mater.* **29** 1805792
[104] Skardal A *et al* 2017 Multi-tissue interactions in an integrated three-tissue organ-on-a-chip platform *Sci. Rep.* **7** 8837

[105] Lai B F L, Huyer L D, Lu R X Z, Drecun S, Radisic M and Zhang B 2017 InVADE: integrated vasculature for assessing dynamic events *Adv. Funct. Mater.* **27** 1703524
[106] Lee J *et al* 2021 A heart-breast cancer-on-a-chip platform for disease modeling and monitoring of cardiotoxicity induced by cancer chemotherapy *Small* **17** 2004258
[107] Novak R *et al* 2020 Robotic fluidic coupling and interrogation of multiple vascularized organ chips *Nat. Biomed. Eng.* **4** 407–20
[108] Herland A *et al* 2020 Quantitative prediction of human pharmacokinetic responses to drugs via fluidically coupled vascularized organ chips *Nat. Biomed. Eng.* **4** 421–36
[109] Digard H, Proctor C, Kulasekaran A, Malmqvist U and Richter A 2012 Determination of nicotine absorption from multiple tobacco products and nicotine gum *Nicotine Tob. Res.* **15** 255–61
[110] Ronaldson-Bouchard K *et al* 2022 A multi-organ chip with matured tissue niches linked by vascular flow *Nat. Biomed. Eng.* **6** 351–71
[111] Giménez-Gómez P, Rodríguez-Rodríguez R, Ríos J M, Pérez-Montero M, González E, Gutiérrez-Capitán M, Plaza J A, Muñoz-Berbel X and Jiménez-Jorquera C 2020 A self-calibrating and multiplexed electrochemical lab-on-a-chip for cell culture analysis and high-resolution imaging *Lab Chip* **20** 823–33
[112] Guo Y, Li H, Reddy K, Shelar H S, Nittoor V R and Fan X 2011 Optofluidic Fabry–Pérot cavity biosensor with integrated flow-through micro-/nanochannels *Appl. Phys. Lett.* **98** 041104
[113] Kim Y, Gonzales J and Zheng Y 2021 Sensitivity-enhancing strategies in optical biosensing *Small* **17** 2004988
[114] Yoon J, Shin M, Lee T and Choi J-W 2020 Highly sensitive biosensors based on biomolecules and functional nanomaterials depending on the types of nanomaterials: a perspective review *Materials* **13** 299
[115] Wang Q, Wang C, Yang X, Wang J, Zhang Z and Shang L 2023 Microfluidic preparation of optical sensors for biomedical applications *Smart Med.* **2** e20220027
[116] Luan J *et al* 2020 Ultrabright fluorescent nanoscale labels for the femtomolar detection of analytes with standard bioassays *Nat. Biomed. Eng.* **4** 518–30
[117] Kang D, Lee S, Shin H, Pyun J and Lee J 2020 An efficient NIR-to-NIR signal-based LRET system for homogeneous competitive immunoassay *Biosens. Bioelectron.* **150** 111921
[118] Xu W *et al* 2020 Diagnosis and prognosis of myocardial infarction on a plasmonic chip *Nat. Commun.* **11** 1654
[119] Liu Y, Dong Y, Jauw J, Linman M J and Cheng Q 2010 Highly sensitive detection of protein toxins by surface plasmon resonance with biotinylation-based inline atom transfer radical polymerization amplification *Anal. Chem.* **82** 3679–85
[120] Gao Z, Ye H, Tang D, Tao J, Habibi S, Minerick A, Tang D and Xia X 2017 Platinum-decorated gold nanoparticles with dual functionalities for ultrasensitive colorimetric *in vitro* diagnostics *Nano Lett.* **17** 5572–9
[121] Odijk M, van der Meer A D, Levner D, Kim H J, van der Helm M W, Segerink L I, Frimat J-P, Hamilton G A, Ingber D E and van den Berg A 2015 Measuring direct current trans-epithelial electrical resistance in organ-on-a-chip microsystems *Lab Chip* **15** 745–52
[122] Srinivasan B, Kolli A R, Esch M B, Abaci H E, Shuler M L and Hickman J J 2015 TEER measurement techniques for *in vitro* barrier model systems *J. Lab. Autom.* **20** 107–26
[123] van der Helm M W *et al* 2019 Non-invasive sensing of transepithelial barrier function and tissue differentiation in organs-on-chips using impedance spectroscopy *Lab Chip* **19** 452–63
[124] Koutsouras D A, Lingstedt L V, Lieberth K, Reinholz J, Mailänder V, Blom P W M and Gkoupidenis P 2019 Probing the impedance of a biological tissue with PEDOT: PSS-coated metal electrodes: effect of electrode size on sensing efficiency *Adv. Healthcare Mater.* **8** 1901215
[125] Marrero D, Guimera A, Maes L, Villa R, Alvarez M and Illa X 2023 Organ-on-a-chip with integrated semitransparent organic electrodes for barrier function monitoring *Lab Chip* **23** 1825–34
[126] Malhotra B D and Ali M A 2018 Nanomaterials in biosensors: fundamentals and applications *Nanomater. Biosens.* **2018** 1–74
[127] Wang L, Han J, Su W, Li A, Zhang W, Li H, Hu H, Song W, Xu C and Chen J 2023 Gut-on-a-chip for exploring the transport mechanism of Hg (II) *Microsyst. Nanoeng.* **9** 2
[128] Mabbott S, Fernandes S C, Schechinger M, Cote G L, Faulds K, Mace C R and Graham D 2020 Detection of cardiovascular disease associated miR-29a using paper-based microfluidics and surface enhanced Raman scattering *Analyst* **145** 983–91
[129] Fernández-Costa J M *et al* 2022 Training-on-a-chip: a multi-organ device to study the effect of muscle exercise on insulin secretion *in vitro Adv. Healthcare Mater.* **8** 2200873
[130] Piloto A M *et al* 2018 Plastic antibodies tailored on quantum dots for an optical detection of myoglobin down to the femtomolar range *Sci. Rep.* **8** 4944
[131] Jeong B, Akter R, Oh J, Lee D-G, Ahn C-G, Choi J-S and Rahman M A 2022 Novel electrochemical PMI marker biosensor based on quantum dot dissolution using a double-label strategy *Sci. Rep.* **12** 8815
[132] Şahin S, Ünlü C and Trabzon L 2021 Affinity biosensors developed with quantum dots in microfluidic systems *Emergent Mater.* **4** 187–209
[133] Biselli E *et al* 2017 Organs on chip approach: a tool to evaluate cancer-immune cells interactions *Sci. Rep.* **7** 1–12
[134] Mencattini A *et al* 2020 Discovering the hidden messages within cell trajectories using a deep learning approach for *in vitro* evaluation of cancer drug treatments *Sci. Rep.* **10** 1–11
[135] Nguyen M *et al* 2018 Dissecting effects of anti-cancer drugs and cancer-associated fibroblasts by on-chip reconstitution of immunocompetent tumor microenvironments *Cell Rep.* **25** 3884–93. e3
[136] Jena B P, Gatti D L, Arslanturk S, Pernal S and Taatjes D J 2019 Human skeletal muscle cell atlas: unraveling cellular secrets utilizing 'muscle-on-a-chip', differential expansion microscopy, mass spectrometry, nanothermometry and machine learning *Micron* **117** 55–59
[137] Stoecklein D, Lore K G, Davies M, Sarkar S and Ganapathysubramanian B 2017 Deep learning for flow sculpting: insights into efficient learning using scientific simulation data *Sci. Rep.* **7** 1–11
[138] Schimek K *et al* 2020 Human multi-organ chip co-culture of bronchial lung culture and liver spheroids for substance exposure studies *Sci. Rep.* **10** 7865